The Astrophysical Journal, 958:109 (16pp), 2023 December 1 https://doi.org/10.3847/1538-4357/acff6e

[C II] Spectral Mapping of the Galactic Wind and Starbursting Disk of M82 with SOFIA

Rebecca C. Levy[1,13], Alberto D. Bolatto[2,3], Elizabeth Tarantino[2,4], Adam K. Leroy[5], Lee Armus[6], Kimberly L. Emig[7,14], Rodrigo Herrera-Camus[8], Daniel P. Marrone[1], Elisabeth Mills[9], Oliver Ricken[10], Juergen Stutzki[11], Sylvain Veilleux[2,3], and Fabian Walter[12]
[1] Steward Observatory, University of Arizona, Tucson, AZ 85721, USA; rebeccalevy@arizona.edu
[2] Department of Astronomy, University of Maryland, College Park, MD 20742, USA
[3] Joint Space-Science Institute, University of Maryland, College Park, MD 20742, USA
[4] Space Telescope Science Institute, 3700 San Martin Drive, Baltimore, MD 21218, USA
[5] Department of Astronomy, The Ohio State University, Columbus, OH 43210, USA
[6] IPAC, California Institute of Technology, 1200 East California Boulevard, Pasadena, CA 91125, USA
[7] National Radio Astronomy Observatory, 520 Edgemont Road, Charlottesville, VA 22903, USA
[8] Departamento de Astronomía, Universidad de Concepción, Barrio Universitario, Concepción, Chile
[9] Department of Physics and Astronomy, University of Kansas, 1251 Wescoe Hall Drive, Lawrence, KS 66045, USA
[10] Max-Planck-Institut für Radioastronomie, Auf dem Hügel 69, D-53121 Bonn, Germany
[11] I. Physikalisches Institut, Universität zu Köln, Zülpicher Straße 77, D-50937 Köln, Germany
[12] Max-Planck-Institut für Astronomie, Königstuhl 17, D-69120 Heidelberg, Germany
Received 2023 April 20; revised 2023 September 26; accepted 2023 September 27; published 2023 November 16

Abstract

M82 is an archetypal starburst galaxy in the local Universe. The central burst of star formation, thought to be triggered by M82's interaction with other members in the M81 group, is driving a multiphase galaxy-scale wind away from the plane of the disk that has been studied across the electromagnetic spectrum. Here, we present new velocity-resolved observations of the [C II] 158 μm line in the central disk and the southern outflow of M82 using the upGREAT instrument on board SOFIA. We also report the first detections of velocity-resolved ($\Delta V = 10$ km s^{-1}) [C II] emission in the outflow of M82 at projected distances of ≈1–2 kpc south of the galaxy center. We compare the [C II] line profiles to observations of CO and H I and find that likely the majority (>55%) of the [C II] emission in the outflow is associated with the neutral atomic medium. We find that the fraction of [C II] actually outflowing from M82 is small compared to the bulk gas outside the midplane (which may be in a halo or tidal streamers), which has important implications for observations of [C II] outflows at higher redshift. Finally, by comparing the observed ratio of the [C II] and CO intensities to models of photodissociation regions, we estimate that the far-ultraviolet (FUV) radiation field in the disk is $\sim 10^{3.5}\ G_0$, in agreement with previous estimates. In the outflow, however, the FUV radiation field is 2–3 orders of magnitudes lower, which may explain the high fraction of [C II] arising from the neutral medium in the wind.

Unified Astronomy Thesaurus concepts: Starburst galaxies (1570); Galaxy winds (626); Interstellar medium (847); Galaxy kinematics (602); Molecular gas (1073); Interstellar atomic gas (833); Far infrared astronomy (529); Infrared galaxies (790)

1. Introduction

Stars inject energy and momentum into their surrounding environments over their entire lifetimes. This so-called stellar feedback can result in massive outflows of gas and dust from the centers of galaxies, where there are high concentrations of stars and star clusters. In these dense environments, energy and momentum injected by supernova explosions and winds from massive stars that are clustered in space and time push material out of the midplane of a galaxy, leading to the observed biconical outflows and superwinds (e.g., Heckman et al. 1990; Veilleux et al. 2005, 2020, and references therein). These outflows are inherently multiphase, with the cool neutral phases of the winds potentially carrying away the bulk of the outflowing mass and the fuel for future star formation (e.g., Veilleux et al. 2020).

The [C II] 158 μm line in the far-infrared (FIR) is one of the brightest lines in star-forming galaxies. It is a major cooling channel of the neutral interstellar medium (ISM) and can contribute 0.1%–1% of the total FIR emission from a galaxy (e.g., Crawford et al. 1985; Stacey et al. 1991). Owing to its low ionization potential (11.2 eV), neutral carbon can be singly ionized in a range of conditions and ISM phases, making the [C II] 158 μm line an excellent tracer of multiphase gas (e.g., Madden et al. 1993; Goldsmith et al. 2012; Pineda et al. 2013). In the disks and centers of nearby star-forming galaxies, [C II] tends to be most closely associated with the neutral atomic component, but a substantial fraction can also arise from the molecular component (Mookerjea et al. 2016; Röllig et al. 2016; Fahrion et al. 2017; Tarantino et al. 2021). It is unknown, however, how the origin and distribution of [C II] may change in a starburst-driven superwind.

M82 is an archetypal starburst galaxy, located at a distance of 3.63 ± 0.34 Mpc (Freedman et al. 1994) in the M81 group. M82 is interacting with the other group members (Yun et al. 1994; de Blok et al. 2018). It is thought that this tidal interaction triggered a central burst of star formation 10 Myr ago, followed by a second bar-driven burst 5 Myr ago (Förster Schreiber et al. 2003). The central starburst has launched a multiphase, galaxy-scale wind, which has been studied across

[13] NSF Astronomy and Astrophysics Postdoctoral Fellow.
[14] Jansky Fellow of the National Radio Astronomy Observatory.

the electromagnetic spectrum (e.g., Lynds & Sandage 1963; Heckman et al. 1990; Strickland et al. 1997; Walter et al. 2002; Engelbracht et al. 2006; Strickland & Heckman 2009; Veilleux et al. 2009; Yoshida et al. 2011, 2019; Yamagishi et al. 2012; Contursi et al. 2013; Beirão et al. 2015; Leroy et al. 2015; Martini et al. 2018; Krieger et al. 2021). It is unclear whether the material in the wind has sufficient energy to escape into the intergalactic medium or whether it will fall back onto the galaxy as a fountain (e.g., Leroy et al. 2015; Martini et al. 2018; Yuan et al. 2023).

Because M82 is such an important laboratory for studying the multiphase ISM in a starburst environment, its center has previously been observed in the [C II] 158 μm line by the Kuiper Airborne Observatory (KAO; Stacey et al. 1991) and Herschel HIFI and PACS (Loenen et al. 2010; Contursi et al. 2013; Herrera-Camus et al. 2018). While the PACS data extend into the base of the outflow, [C II] has not been detected in the outflow at distances greater than $\sim$1 kpc from the midplane. Moreover, because of the low velocity resolution of PACS, the [C II] data from that instrument are not velocity-resolved.

In this paper, we present new observations of the [C II] 158 μm line taken with the upgraded German REceiver for Astronomy at Terahertz Frequencies (upGREAT; Risacher et al. 2018) on board the Stratospheric Observatory for Infrared Astronomy (SOFIA; Temi et al. 2018). These velocity-resolved observations measured [C II] at 10 km s^{-1} velocity resolution in the inner disk of M82 and the southern side of the superwind at distances of 1–2 kpc from the midplane.

This paper is organized as follows. We describe the data used in this study in Section 2. In Section 3, we discuss the main results from the [C II] detections in the outflow of M82. The main results from the [C II] map in the disk are discussed in Section 4. A discussion of the disk and wind together is presented in Section 5. We discuss constraints on the far-ultraviolet (FUV) radiation field in both the disk and outflow in Section 6. We summarize our main conclusions in Section 7.

Throughout, we use CO to refer to $^{12}C^{16}O(J = 1–0)$. We use $(\alpha, \delta) = (09^h55^m52\overset{s}{.}72, +69°40^m45\overset{s}{.}8)$ as the J2000 R.A. and decl. of the center of M82 (Martini et al. 2018). We assume a central recessional velocity of 210 km s^{-1} in the LSRK (Krieger et al. 2021). We assume that the position angle[15] (PA) of M82 is 67°; therefore, the PA of the southern side of the wind is 157° (e.g., Martini et al. 2018). We adopt an inclination of 80° for the disk (e.g., Lynds & Sandage 1963; McKeith et al. 1993; Martini et al. 2018; Krieger et al. 2021). The data and code for the analysis presented here are available in Zenodo (Levy 2023).[16]

2. Observations and Data Reduction

2.1. [C II] Data from upGREAT

These observations of the [C II] 158 μm line in M82 were taken using the low-frequency array (LFA) of the upGREAT[17] instrument (Risacher et al. 2018) on board SOFIA (Temi et al. 2018). These data were taken in cycle 8 as part of project 08_0225 (PI: R. Levy) on 2021 February 19, February 23, February 25, March 10, and March 11.

The upGREAT LFA consists of a seven-pixel hexagonal array for each polarization; the polarizations were averaged for these data. It was tuned to the [C II] line at 158 μm (1.9005 THz). At this frequency, each upGREAT LFA pixel has a half-power beamwidth of 14.″1 ($\approx$250 pc). The bandwidth of the observations ranged from -150 to 430 km s^{-1} (1.8996$-$1.9033 THz, $\Delta\nu = 3.6$ GHz), with a native velocity resolution of 0.04 km s^{-1} ($R \approx 7.5 \times 10^6$).

The observing time was split between making an on-the-fly (OTF) map of the inner $3' \times 1'$ of the disk and a single pointing of the upGREAT LFA along the southern outflow. Both observing strategies used a dual-beam-switching mode to measure the OFF positions to maximize baseline stability. More details pertaining to the OTF map and single pointing are given in Sections 2.1.1 and 2.1.2. The footprints of the OTF map and single pointing are shown in Figure 1.

All observations were pipeline-calibrated (in particular: correction for atmospheric transmission) with the GREAT *kalibrate* software (Guan et al. 2012) by the upGREAT team and further processed to level-2 data using the CLASS software in GILDAS. As part of the calibration, a first-order baseline was removed, the final spectra were smoothed to 10 km s^{-1} channels, and the spectra were converted to a main-beam temperature (T_{mb}) scale, where $\eta_{mb} \approx 0.67$.

2.1.1. Disk Map

To map the inner region of the disk, the LFA was scanned across the central $4.'3 \times 2.'3$, centered on the galaxy center given in Section 1, at an angle of $-20°$ so that the long axis of the map is aligned with the galaxy's major axis. With this strategy, the fully sampled region of the map covers the inner $3.'1 \times 1.'1$ (3 kpc $\times$ 1 kpc) as shown in Figure 1. Two tunings (centered at 250 km s^{-1} and 290 km s^{-1} LSRK) were used to capture the full extent of the [C II] emission in the disk. The spectra were weighted by $1/\sigma^2_{rms}$, where σ_{rms} is the rms noise of the baseline. The 3D data cube of the disk has an rms noise of 307 mK in 10 km s^{-1} channels away from the emission. Spatial pixels are $7'' \times 7''$ and hence oversample the beam by a factor of $\approx$3 (in area).

We make 2D maps of the [C II] peak intensity, integrated intensity, mean velocity, and line width using moments.[18] We restrict the velocity range to -100–400 km s^{-1} in the calculation of these quantities. For the disk maps, we mask out elements in the cube where the intensity is less than $2\times$ rms noise ($2 \times 307 = 614$ mK). These moment maps are shown in Figure 2, with the integrated intensity map also being shown in Figure 1.

As noted in Section 1, the [C II] 158 μm line has been previously observed in the center of M82 using the KAO (Stacey et al. 1991), Herschel PACS (Contursi et al. 2013; Herrera-Camus et al. 2018), and HIFI (Loenen et al. 2010). In this article, we compare the upGREAT map to that from PACS (Contursi et al. 2013).[19] To robustly compare these measurements, we convolve the PACS cube to the 14″ Gaussian beam of upGREAT using the kernels provided by Aniano et al. (2011). In single beams (not maps), Tarantino et al. (2021)

[15] The PA is measured counterclockwise from north to the receding side of the major axis of the galaxy.

[16] See also https://github.com/rclevy/M82_CII.

[17] upGREAT is a development by the MPI für Radioastronomie and KOSMA/Universität zu Köln, in cooperation with the MPI für Sonnensystemforschung and the DLR Institut für Optische Systeme.

[18] In both the disk and outflow, the [C II] lines are often not Gaussian and so deriving these quantities using a Gaussian fit may lead to biased results.

[19] The level-2 PACS data were downloaded from the Herschel Science Archive, observation ID 1342187205.

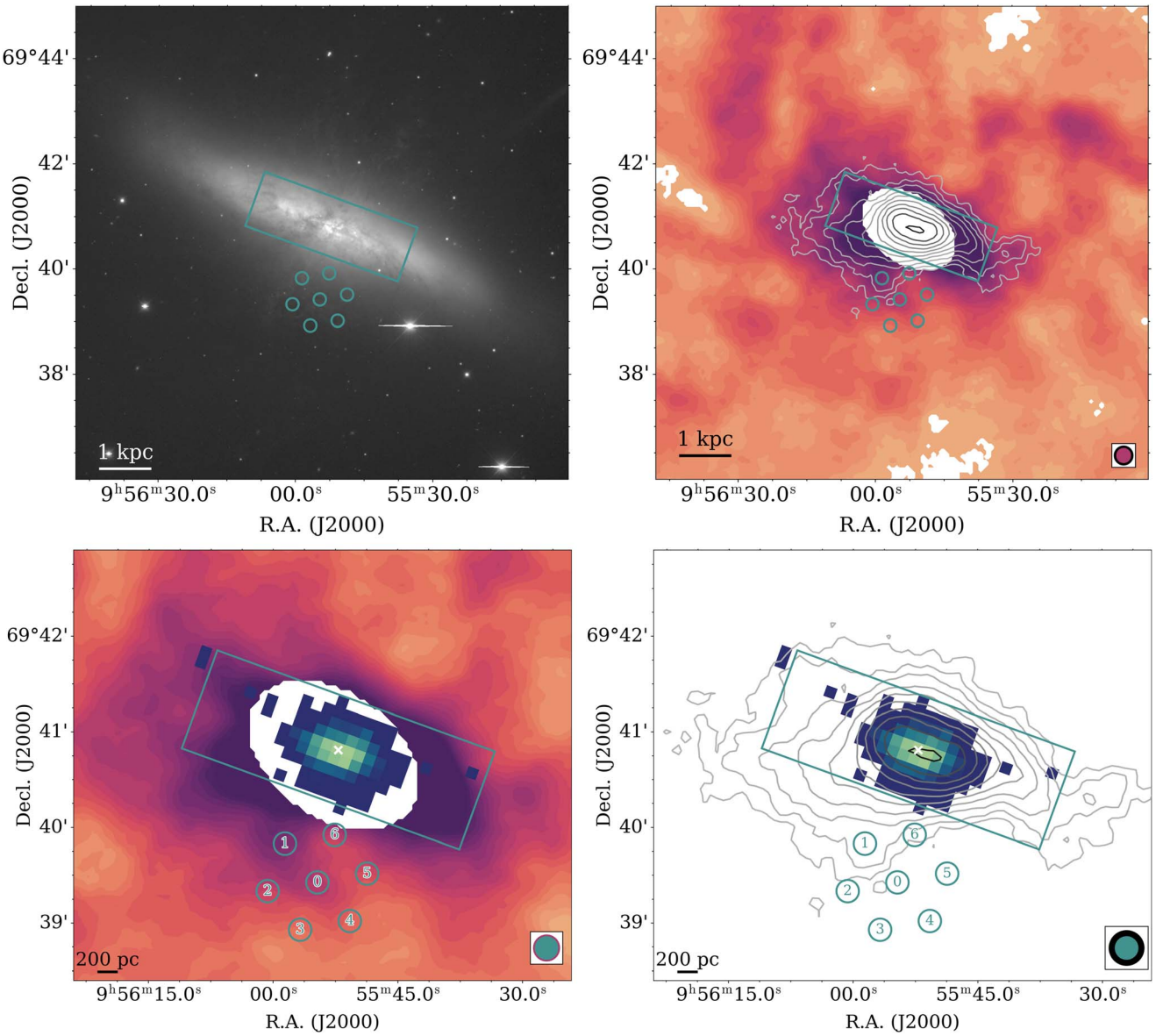

Figure 1. Composite maps of M82. In all panels, the teal rectangle shows the fully sampled region of the upGREAT [C II] map of the disk (3 kpc × 1 kpc). The footprints of the upGREAT single pointing along the southern outflow are shown as the teal circles, where the size of each circle is the upGREAT beam size (14.″1). Top left: an *r*-band image of M82 from the SINGS Survey (Kennicutt et al. 2003). Top right: the H I integrated intensity is shown by orange–purple filled contours, with values linearly spanning 4–1500 K km s^{-1} (Martini et al. 2018). The missing H I data in the center reflect where accurate H I information cannot be obtained due to strong absorption against the continuum; this region fully covers the region detected with signal-to-noise ratio (S/N) >2 in the [C II] map. The CO integrated intensity is shown by grayscale contours, with values logarithmically spanning 20–600 K km s^{-1} (Krieger et al. 2021). The FWHM beam sizes of the H I and CO data are shown in the lower right corner in magenta and black respectively. Bottom left: a zoom-in, showing the [C II] integrated intensity in green–blue, with values logarithmically spanning 200–1200 K km s^{-1}. The H I integrated intensity is shown by the orange–purple filled contours over the same range of values as in the top right panel. The FWHM beam sizes of the H I and [C II] data are shown in the lower right corner in magenta and teal respectively. The numbers in each of the teal circles give the pixel numbers of the LFA. The white × marks the galaxy center. Bottom right: the same as the bottom left, but showing the CO integrated intensity (as grayscale contours over the same range of values as in the top right panel) instead of the H I.

found that not properly accounting for the different shapes of the point-spread function (PSF) can lead to 40% discrepancies between fluxes measured by PACS and upGREAT. We compute the integrated intensity using a moment analysis over the same velocity range as the upGREAT data. We measure the flux from the matched upGREAT and PACS maps in a $1' \times 1'$ box (rotated by $-20°$) centered on the center of M82 (Martini et al. 2018). This box optimizes the overlapping regions of the upGREAT and PACS maps. Over this region, the integrated [C II] line intensity measured from the upGREAT map is 2.0×10^{-13} W m^{-2}. The matched PACS map yields 1.9×10^{-13} W m^{-2}. These two values agree to within 5%, well within the 30% PACS calibration uncertainty (Contursi et al. 2013).

2.1.2. Outflow Pointings

To measure [C II] in the outflow, a single pointing of the upGREAT LFA was used. A location on the southern (brighter) side of the outflow was chosen such that the central pixel of the upGREAT array (pixel 0) was located 1.5 kpc from the galaxy center along the outflow (i.e., the galaxy minor axis with PA = 157°). The LFA array was rotated by 70° to maximize the extent along the southern outflow. The footprint

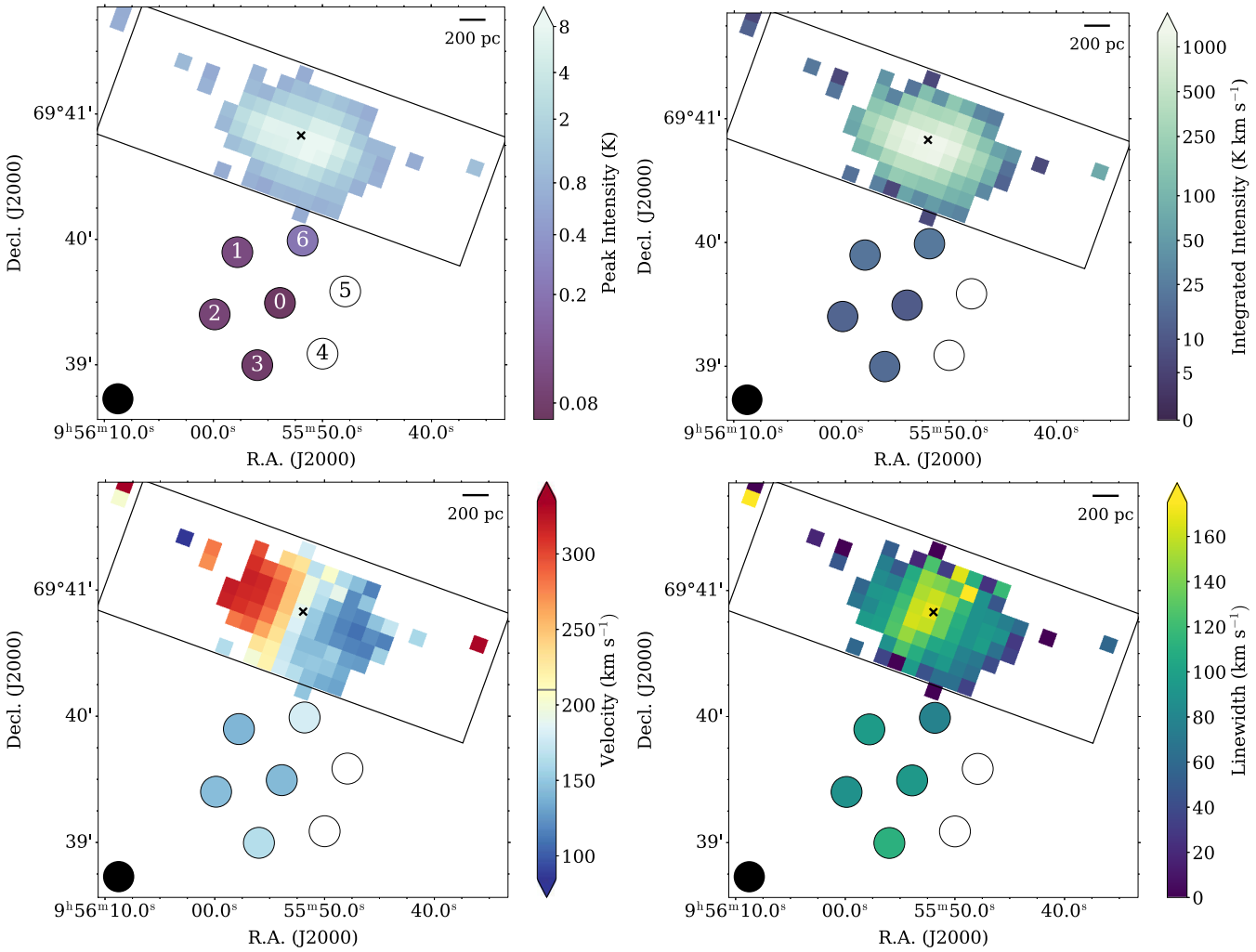

Figure 2. The upGREAT [C II] maps of the central 3 kpc × 1 kpc of M82, showing the [C II] peak intensity (top left), integrated intensity (moment 0; top right), mean velocity (moment 1; bottom left), and line width (moment 2; bottom right). Spaxels with S/N < 2 (relative to the rms noise of the cube) are masked out of the 3D cube before the 2D maps are made. The black rectangle shows the boundaries of the fully sampled map. The black-outlined circles below the maps show the same values for the single pointings along the outflow. The numbers in each of the circles in the upper left panel give the pixel numbers of the LFA. The solid black circles in the lower left corners show the 14.″1 (≈250 pc) beam. The black × marks the galaxy center (Martini et al. 2018). In the lower left panel, the gray horizontal line in the color bar marks the systemic velocity (V_{sys}) of M82 (210 km s^{-1}; Krieger et al. 2021).

of the LFA is shown is Figures 1 and 2. The spectra in the outflow, shown in Figure 3, have rms noise of 7–12 mK in 10 km s^{-1} channels.

We calculate moments of the spectra to measure the peak and integrated intensity, the mean velocity, and the line width. As with the disk map, we restrict the velocity range to −100–400 km s^{-1} in the calculation of these quantities. We report these values in Table 1 and show these quantities in Figure 2.

As a check, we compare the flux we measure in outflow pixels 1 and 6 to the Herschel PACS map (Contursi et al. 2013) convolved to a 14″ Gaussian PSF as described in Section 2.1.1. Pixels 1 and 6 are the only upGREAT pointings that overlap with the PACS coverage. From the PACS map, we measure a total [C II] integrated line intensity of 4.8 K km s^{-1} (12.0 K km s^{-1}) in pixel 1 (6). This is lower than the [C II] integrated intensity of 21.2 K km s^{-1} (23.3 K km s^{-1}) measured in the upGREAT map (Table 1). We note, however, that these pixels are at the edges of the PACS map and there may be substantial flux loss due to edge effects and undersampling. When these PACS maps were reprocessed by Herrera-Camus et al. (2018), for example, these edge regions were excluded.

2.2. Ancillary Data

Because [C II] can be excited in many conditions, we compare the [C II] emission with the molecular and atomic ISM components. We use ancillary CO and H I data as tracers of those respective components.

2.2.1. CO(1–0) Tracing the Molecular Gas

The CO data used in this study are from the Institut de Radioastronomie Millimétrique (IRAM) 30 m telescope. These data were presented by Krieger et al. (2021), and we direct the reader to that paper for details on the observations, calibration, and imaging. We note that while the data presented by Krieger et al. (2021) include both interferometric and single-dish observations, we find that there are significant interferometric artifacts (absorption) in the spectra that hinder the comparison to the [C II] data in this work. Therefore, we use only the single-dish data, which do not show these spectral artifacts. The

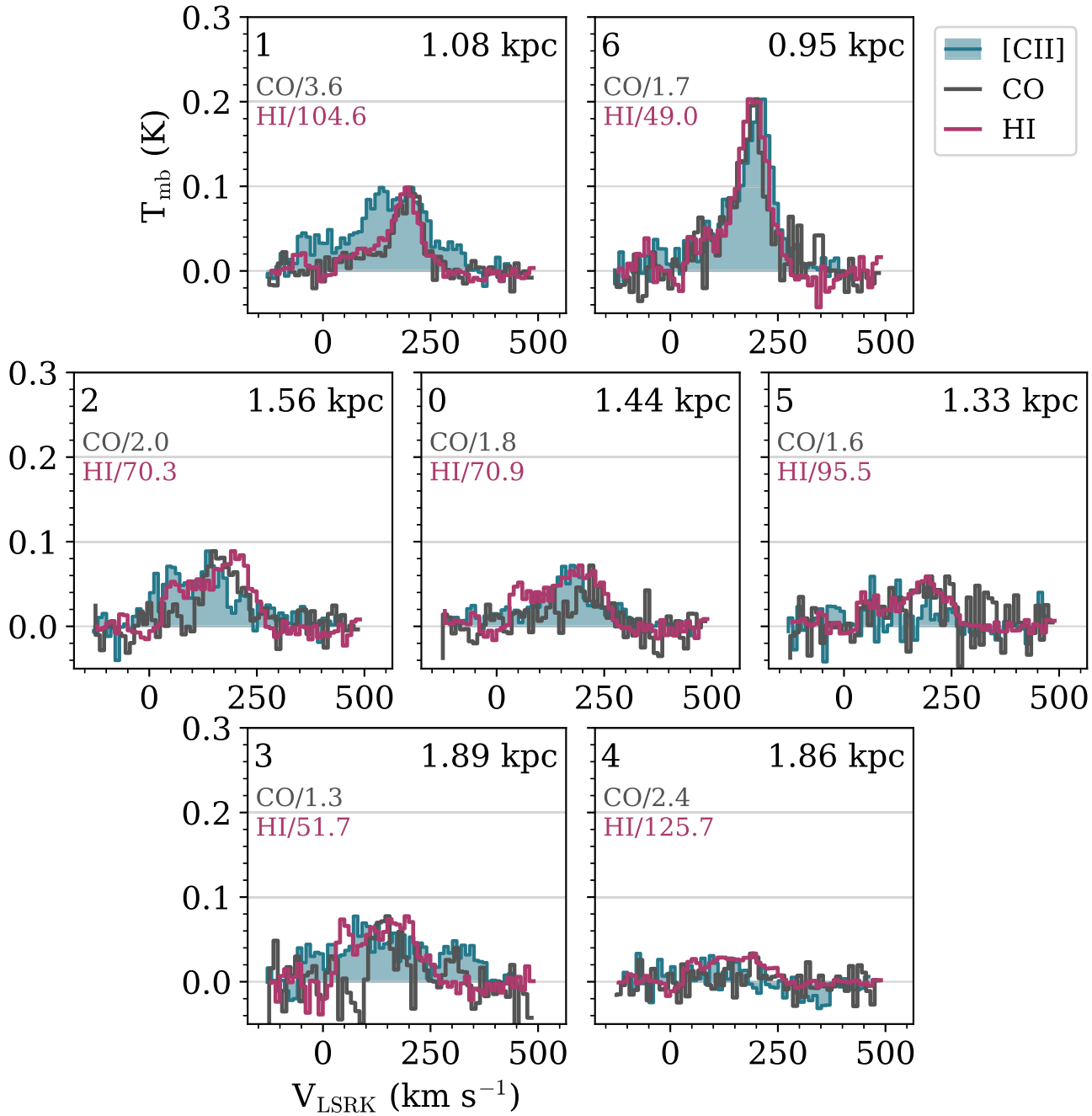

Figure 3. SOFIA upGREAT [C II] spectra in the southern outflow of M82, with 10 km s^{-1} channels (teal filled). The panels are arranged as shown in Figure 1, where the pixel number is shown in the top left of each panel. The distance from the center of each LFA pixel to the galaxy center is shown in the top right corner. The panels all have the same axis scaling, as shown in the lower left panel. Scaled versions of the CO (dark gray) and H I (magenta) profiles are overplotted. The CO and H I spectra are simply normalized to the peak of the [C II] spectrum, and the values by which the CO and H I spectra are scaled are listed in each panel.

final CO cube has a spatial resolution of 22″ (≈385 pc) and a velocity resolution of 5 km s^{-1}. For this work, we smooth the CO cube to a velocity resolution of 10 km s^{-1} to match the [C II] data. We show the CO integrated intensity in Figure 1.

2.2.2. H I Tracing the Atomic Gas

The H I data used in this study are from the Karl G. Jansky Very Large Array (VLA) and have been combined with single-dish data from the Robert C. Byrd Green Bank Telescope (GBT). These data were presented by Martini et al. (2018), and we direct the reader to that paper for details on the observations, calibration, and imaging. The H I cube has a native velocity resolution of 5 km s^{-1}. We spectrally smooth these data to a velocity resolution of 10 km s^{-1} to match the [C II] data. The H I data used here have a spatial resolution of 17″ (≈300 pc), slightly higher than that presented by Martini et al. (2018). In the center of M82, the H I is heavily absorbed against the bright continuum (Martini et al. 2018), so the H I cannot be compared to the [C II] in the disk; this is not a problem in the outflow pointings. To produce the integrated intensity map (Figure 1), we create a mask to exclude the absorption and to exclude channels where the H I intensity is <2.3 K (S/N < 3). We note that our analysis is performed on the H I cube itself, and the H I integrated intensity map is to aid in the visualization.

Table 1
Properties of [C II] Spectra in the Outflow

Pixel Number	R.A. (J2000)	Decl. (J2000)	I_{peak} (mK)	I_{int} (K km s^{-1})	V_0 (km s^{-1})	σ_V (km s^{-1})	Rms (mK)	$\log_{10}(M_{C^+}/M_\odot)$
0	$9^h55^m54\overset{s}{.}6$	$+69°39'24\overset{''}{.}3$	72.0 ± 14.8	10.8 ± 1.0	143.3 ± 10.2	94.2 ± 16.9	5.8	3.5 ± 0.2
1	$9^h55^m56\overset{s}{.}2$	$+69°39'46\overset{''}{.}9$	98.6 ± 33.4	21.2 ± 2.4	141.2 ± 10.3	96.0 ± 19.7	9.4	3.8 ± 0.1
2	$9^h55^m56\overset{s}{.}9$	$+69°39'19\overset{''}{.}8$	88.9 ± 28.2	13.7 ± 2.0	144.9 ± 10.5	89.3 ± 17.5	9.6	3.6 ± 0.2
3	$9^h55^m55\overset{s}{.}3$	$+69°38'59\overset{''}{.}1$	77.5 ± 31.0	16.4 ± 2.2	165.1 ± 10.6	111.8 ± 93.8	6.9	3.7 ± 0.1
4	$9^h55^m53\overset{s}{.}4$	$+69°39'00\overset{''}{.}0$	…	…	…	…	6.8	…
5	$9^h55^m52\overset{s}{.}5$	$+69°39'30\overset{''}{.}1$	…	…	…	…	16.8	…
6	$9^h55^m54\overset{s}{.}1$	$+69°39'52\overset{''}{.}3$	203.0 ± 27.4	23.3 ± 1.9	180.2 ± 10.3	77.4 ± 247.0	11.5	3.8 ± 0.1

Note. The R.A. and decl. of the center of each pixel are given. The other columns show the moments of the spectra including the peak intensity (I_{peak}), the integrated intensity (moment 0; I_{int}), the mean velocity (moment 1; V_0), the line width (moment 2, σ_V), and corresponding uncertainties. The moments are calculated over a fixed velocity range spanning −100–400 km s^{-1}. Rms is the rms noise of the spectrum calculated outside of the velocity range used for the moments. If the moments cannot be calculated because the line is not detected, then the rms is calculated over the entire bandpass. All temperatures refer to T_{mb}. M_{C^+} is the mass in C^+ inferred from the spectrum considering only collisions with the atomic gas; see the Appendix for details of this calculation.

2.2.3. r-band Image

For visualization purposes, we show an *r*-band image of M82 in Figure 1. This image was taken as part of the SINGS Survey (Kennicutt et al. 2003; SINGS Team 2020) and was downloaded from the NASA/IPAC Extragalactic Database.

2.2.4. Matching the Data Sets

In the outflow, we extract the CO and H I from the central pixel of each upGREAT pointing. As noted above, the CO and H I data are smoothed to a velocity resolution of 10 km s^{-1}, to match the [C II]. To make the most accurate comparison, the data should be convolved to the 22″ resolution of the CO data. Because, however, the upGREAT data in the outflow are single pointings (not a map), they cannot be convolved to lower resolution. Therefore, we do not match the beam sizes of the CO, H I, and [C II] data in the outflow. As we will discuss in Section 4, we do match the resolutions and pixel scales of the [C II] and CO data sets in the disk.

We show the [C II], CO, and H I spectra in Figure 3, where the CO and H I are simply normalized to the peak intensity of the [C II]. We derive the CO and H I integrated intensities (moment 0) in the same way as for the [C II] spectra and over the same velocity range. In Table 2, we give the ratios of the integrated intensities of H I/[C II] and CO/[C II], where all integrated intensities are in units of K km s^{-1}.

Table 2
Ratios of the Integrated Intensities and Luminosities in the Outflow

Pixel Number	$I_{int,H\ I}/I_{int,[C\ II]}$	$I_{int,CO}/I_{int,[C\ II]}$	$L_{[C\ II]}/L_{CO}$
0	1372.9 ± 140.5	12.0 ± 1.3	154 ± 6
1	779.1 ± 91.1	12.0 ± 1.4	154 ± 6
2	944.4 ± 141.2	11.4 ± 1.7	163 ± 7
3	498.5 ± 69.5	3.5 ± 0.5	535 ± 30
4	…	…	…
5	…	…	…
6	718.3 ± 65.7	14.8 ± 1.3	125 ± 5

Note. To form the ratios, all integrated intensities are in units of K km s^{-1} and all luminosities are in units of $L_\odot$.

3. [C II] in the Wind of M82

We robustly detect the [C II] 158 μm line in five of the seven LFA pixels in the southern outflow of M82, as shown in Figure 3. As described in Section 2.1.2, we calculate moments of these spectra, which are listed in Table 1 and shown in Figure 2. The ratios of the peak CO to [C II] intensities (in brightness temperature units of kelvin) are ∼1, in agreement with previous work (Stacey et al. 1991). We present the integrated intensity ratios (on an intensity scale of K km s^{-1}) in each LFA pixel in Table 2.

From the [C II] spectra in the outflow, we calculate the column density and mass of C^+ in each outflow pointing. These calculations are detailed in the Appendix. Briefly, the C^+ column density as a function of velocity (N_{C^+}) is calculated the following Equation (A5), assuming that the [C II] is only excited in the cold neutral medium (CNM; e.g., Pineda et al. 2013; Fahrion et al. 2017; Herrera-Camus et al. 2017). For this calculation, we must assume a kinetic temperature, *T*, and a gas density, *n*. Our assumed temperature and density come from inspecting the spatially resolved results of modeling the photodissociation region (PDR) presented by Contursi et al. (2013). Though they do not probe as far into the outflow as our measurements, they find temperatures of $T \sim 200$–300 K and densities of $n \sim 10$–150 cm^{-3} along the southern outflow away from the disk (uncorrected for the effects of the ionized gas; see their Figures 15 and 16). We note that these values differ from those presented in their Table 1. The "southern outflow" macro region they define is likely contaminated by the starburst (see their Figure 18) and hence the average temperature and density reported in that table are likely too high to apply to the part of the outflow we are studying. From these results, we take a representative temperature of $T = 250 \pm 50$ K and a representative density of $n = 100 \pm 50$ cm^{-3}.

As we discuss in more detail below, our choice to assume that the [C II] is primarily excited in the CNM is well justified. We sum this column density over velocity and multiply by the area of each LFA pixel to measure the mass in C^+ (M_{C^+}; Equation (A11)). We list M_{C^+} in each pointing in Table 1. The total C^+ mass in the part of the outflow covered by these pointings is $2.4 \times 10^4\ M_\odot$ (excluding pixels 4 and 5, where the [C II] line is not detected).

3.1. Atomic Gas in the Outflow

From N_{C^+}, we can estimate the effective CNM column density needed to produce the observed [C II] spectra (see details in Appendix A.1). To make this conversion, we divide N_{C^+} by a C/H abundance ratio (C/H = 1.5×10^{-4}; Gerin et al.

2015). We show these effective CNM column density profiles (per unit velocity, i.e., divided by the channel width of 10 km s^{-1}) based on the [C II] ($N_{\rm CNM}^{\rm [C\,II]}$) in teal in Figure 4.

In order to determine the ISM phase from which most of the [C II] emission originates, we compare our $N_{\rm CNM}^{\rm [C\,II]}$ profiles to the measured profiles of total H I column density ($N_{\rm H\,I}$). Modulo optical depth effects, the H I profiles (measured directly from the H I data) probe the total atomic gas content from both the CNM and the warm neutral medium (WNM). Following Martini et al. (2018), we convert the H I intensity to a column density where

$$N_{\rm H\,I} = 1.823 \times 10^{18} \left[\frac{I_{\rm H\,I}}{\rm K\ km\ s^{-1}} \right] \quad {\rm cm\ s^{-2}} \qquad (1)$$

which assumes optically thin emission. These column density profiles (per unit velocity) are shown in magenta in Figure 4. For all LFA pixels, $N_{\rm H\,I} > N_{\rm CNM}^{\rm [C\,II]}$, meaning there is sufficient H I to fully explain the [C II] emission without the need to invoke optical depth effects.

A somewhat more direct comparison of the column densities can be made by assuming some CNM fraction ($f_{\rm CNM}$) of the atomic component, since the [C II] emission is thought to arise only from the cold phase (e.g., Pineda et al. 2013; Fahrion et al. 2017; Herrera-Camus et al. 2017). In Figure 4, we show $N_{\rm CNM}^{\rm HI} \equiv f_{\rm CNM} N_{\rm H\,I}$ for $f_{\rm CNM} = 0.5$ (thin magenta lines). In all LFA pixels, $N_{\rm CNM}^{\rm HI} \gtrsim N_{\rm CNM}^{\rm [C\,II]}$, meaning that there is enough CNM to fully explain all of the [C II] emission. The ratio of $N_{\rm CNM}^{\rm HI}$ to $N_{\rm CNM}^{\rm [C\,II]}$ at the peak of the H I profile is given in the upper right of each panel in Figure 4. By varying $f_{\rm CNM}$, we find that the [C II] emission can be fully explained by collisions with the atomic gas for $f_{\rm CNM} > 0.2$.

To assess the impact of uncertainties in our assumed temperature and density, we perform a Monte Carlo analysis over both quantities. Using 500 trials, we allow both T and n to vary uniformly over the uncertainty range when calculating the column density. We define the uncertainty on the column density as the standard deviation of the trials. We propagate this uncertainty through to the ratio shown in the upper right of each panel in Figure 4.

There is evidence of a warm atomic phase in some of the spectra. Focusing specifically on pixel 1, the [C II] profile is more "flat-topped" than the H I (both in Figures 3 and 4). This peak in the H I profile around $V_{\rm LSRK} = 200$ km s^{-1} may be indicative of an appreciable WNM component. A similar WNM component is seen in pixel 2 at a similar velocity. In pixel 6, however, the atomic gas appears to be dominated by a cold component. Thus there are variations in the overall density and temperature of the atomic component within the outflow of M82, likely because the entrained material is clumpy.

3.2. Molecular Gas in the Outflow

As the [C II] emission can also arise from the molecular phase, we also calculate $N_{\rm C^+}$ assuming collisions with only H_2 (see details in Appendix A.2). We assume the same temperature and density as for collisions with the atomic gas and we assume an abundance ratio of $\rm C/H_2 = 2 \times C/H = 3.0 \times 10^{-4}$. We show these effective H_2 column density profiles (per unit velocity) based on the [C II] ($N_{\rm H_2}^{\rm [C\,II]}$) in teal in Figure 5. We repeat the Monte Carlo analysis over the uncertainties in T and n as above.

To compare, we calculate the column density of H_2 from the CO data ($N_{\rm H_2}^{\rm CO}$). To convert from the CO intensity to column density (per unit velocity), we assume a "starburst" CO-to-H_2 conversion factor $X_{\rm CO} = 0.5 \times 10^{20}$ cm^{-2} (K km s^{-1})$^{-1}$ (e.g., Bolatto et al. 2013; Krieger et al. 2021). The value is slightly smaller than the single value of $X_{\rm CO} = 0.7 \times 10^{20}$ cm^{-2} (K km s^{-1})$^{-1}$ used by Leroy et al. (2015), where we have converted from CO(2–1) to CO(1–0) assuming $I_{\rm CO\,2-1}/I_{\rm CO\,1-0} = 0.7$. In their model of M82, Yuan et al. (2023) find $X_{\rm CO} \approx 0.2 \times 10^{20}$ cm^{-2} (K km s^{-1})$^{-1}$ for this region of the southern outflow.[20]

We show these molecular gas column density profiles in gray in Figure 5, assuming our fiducial $X_{\rm CO} = 0.5 \times 10^{20}$ cm^{-2} (K km s^{-1})$^{-1}$. We note that adopting the conversion factors used by Leroy et al. (2015) or Yuan et al. (2023) produces negligible changes in the $N_{\rm H_2}^{\rm CO}$ profiles. In all LFA pixels, $N_{\rm H_2}^{\rm CO} \sim 15\%$–$40\%\ N_{\rm H_2}^{\rm [C\,II]}$, with most pixels $\sim$20%, meaning that the molecular gas (traced by CO) is not the dominant contributor to the overall [C II] emission. In summary, because only $\sim$20% of the [C II] can be excited by the molecular ISM, we conclude that the majority of the [C II] arises from the CNM. This result has important connections to studies of [C II] in dusty star-forming galaxies at higher redshifts, where the [C II] 158 μm line is visible with interferometers such as the Atacama Large Millimeter/submillimeter Array (ALMA). While it is tempting to use the [C II] lines as a tracer of molecular gas and star formation rate (e.g., Herrera-Camus et al. 2015; Zanella et al. 2018; Dessauges-Zavadsky et al. 2020), caution should be used as these results in M82 suggest that the majority of the [C II] does not arise from the molecular, star-forming material.

3.2.1. CO-dark Molecular Gas

CO does not perfectly trace the total molecular gas content of the ISM, and this component of missed gas is called CO-dark molecular gas (e.g., Grenier et al. 2005; Langer et al. 2010; Wolfire et al. 2010). By its nature, this phase is difficult to study. In the Milky Way, the fraction of molecular gas not traced by CO varies with galactocentric radius and cloud density, dropping below 20% within 4 kpc of the center and in dense clouds, but reaching nearly 80% in the diffuse ISM and beyond 10 kpc (Pineda et al. 2013; Langer et al. 2014). From their models, Wolfire et al. (2010) found that the fraction of CO-dark gas in PDRs is relatively constant with the ambient radiation field and that the main driver is the cloud's visual extinction, A_V—a measure of the dust shielding—where the fraction of CO-dark molecular gas decreases steeply with increasing A_V. The fraction of CO-dark molecular gas increases at lower metallicity as the CO molecule is more easily dissociated due to a lack of shielding dust (e.g., Wolfire et al. 2010; Bolatto et al. 2013).

Applying these previous results to the starburst-driven outflow of M82, we would expect a low CO-dark molecular gas fraction. The metallicity in this region is solar (or slightly supersolar; e.g., Lopez et al. 2020). At the resolution of these upGREAT observations, A_V will vary substantially within a beam. Over their entire field of view, which mainly covers the central starburst, Förster Schreiber et al. (2001) found $A_V = 36 \pm 16$ mag. Extending the models from Wolfire et al. (2010) would imply a CO-dark gas

[20] In their Figure 13, Yuan et al. (2023) report $X_{\rm CO\,2-1}$. We have converted this to $X_{\rm CO\,1-0}$ assuming $I_{\rm CO\,2-1}/I_{\rm CO\,1-0} = 0.7$ (Leroy et al. 2015).

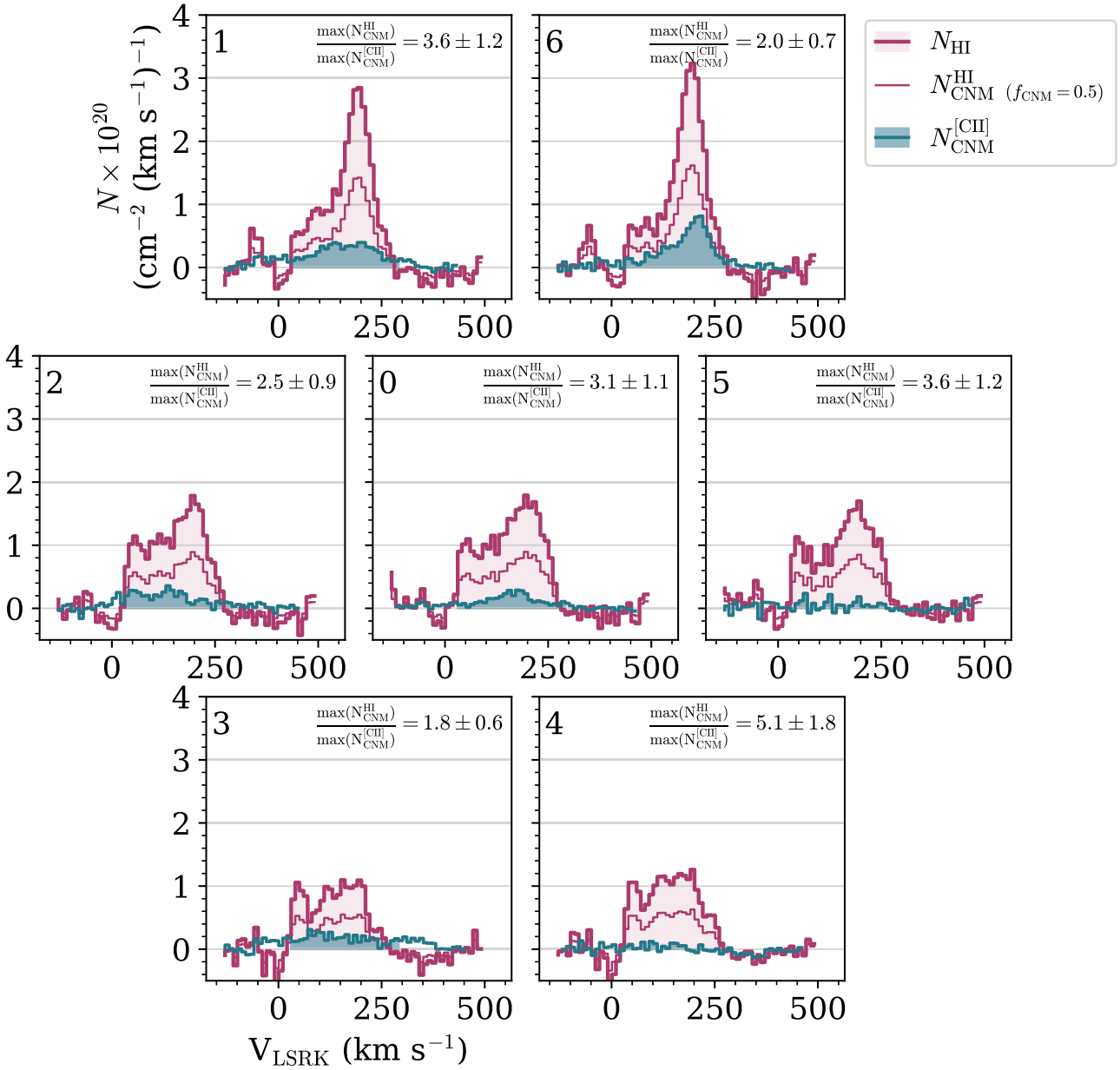

Figure 4. The H I and CNM column densities (per unit velocity) in the outflow of M82. The teal curves show the CNM column density inferred from the [C II] spectrum ($N_{CNM}^{[C\,II]}$) assuming collisions with only the atomic gas, $T = 250$ K, $n = 100$ cm^{-3}, and C/H $= 1.5 \times 10^{-4}$. The thick magenta curves show $N_{H\,I}$ measured directly from the H I data. The thin magenta curves show the CNM column density inferred from the H I (N_{CNM}^{HI}) assuming $f_{CNM} = 0.5$. The LFA pixels are oriented as in Figure 3, and the pixel numbers are given in the top left corner of each panel. The number in the top right corner of each panel is the ratio of the peaks of N_{CNM}^{HI} and $N_{CNM}^{[C\,II]}$ over the shaded portions of the profiles. The uncertainties come from a Monte Carlo analysis over the range of temperatures and densities considered.

fraction of ∼10%–25%. Because the shielding by dust is likely lower in the outflow than in the nucleus, we estimate that ∼25% of the molecular gas may be in a CO-dark phase. Combining this with the fraction of the [C II] line attributed to the CO-emitting molecular gas (∼20%), we would expect a ∼5% contribution to the total [C II] line from CO-dark molecular gas.

3.3. Ionized Gas in the Outflow

The [C II] line can also be excited in the ionized phase of the ISM. It is thought that, when [C II] is excited in ionized conditions, the majority of the [C II] emission arises from regions of diffuse ionized gas rather than H II regions (e.g., Nagao et al. 2011; Contursi et al. 2013). In the KINGFISH sample, Croxall et al. (2017) found that 25% ± 8% of the [C II] is associated with the ionized gas. In star-forming regions in the center of the Milky Way, Harris et al. (2021) found that PDRs and H II regions contribute roughly equally to the [C II] flux. Therefore, while it is likely that the fraction of [C II] associated with the ionized gas changes with environment, the ionized ISM is not the dominant contributor to the [C II] emission.

Contursi et al. (2013) found that the ionized gas traced by Hα in the outflow of M82 is kinematically decoupled from the neutral (atomic and molecular) phases and from ionized gas traced by [O III] 88 μm emission. Moreover, they found that the ionized and neutral phases may not be co-spatial in the outflow. They proposed a scenario where the Hα-emitting ionized gas is more extended, is confined to the walls of the biconical outflow, has a higher outflow velocity (∼600 km s^{-1}), and is ionized (at least in part) by shocks between the outflowing

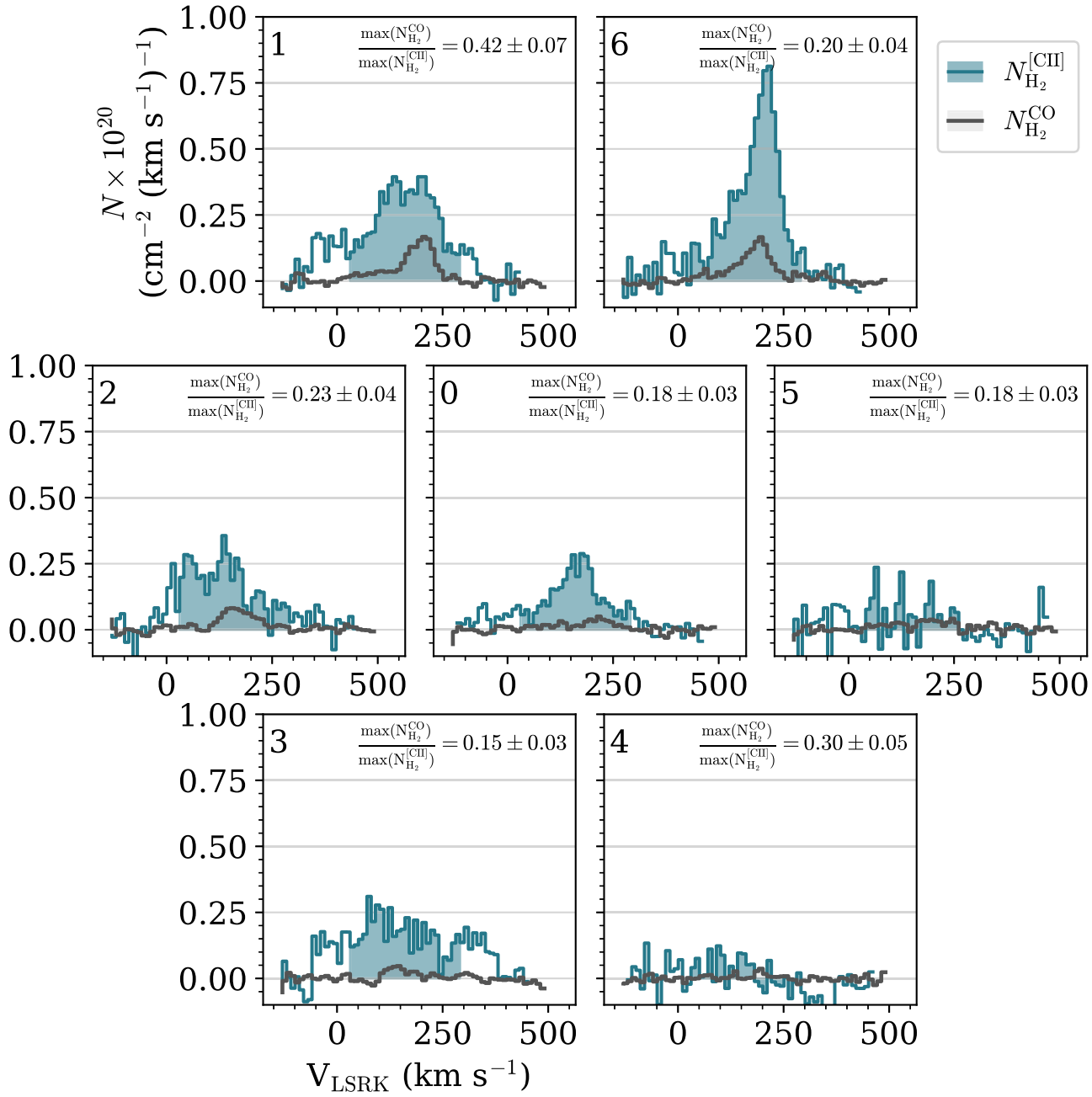

Figure 5. Similar to Figure 4, but showing the H_2 column densities (per unit velocity) in the outflow of M82. The teal curves show the H_2 column density inferred from the [C II] spectrum ($N_{H_2}^{[C\,II]}$) assuming collisions with only H_2, $T = 250$ K, $n = 100$ cm^{-3}, and $C/H_2 = 3 \times 10^{-4}$. The gray curves show the column density of H_2 measured from the CO data ($N_{H_2}^{CO}$) assuming $X_{CO} = 0.5 \times 10^{20}$ cm^{-2} (K km s^{-1})$^{-1}$. The number in the top right corner of each panel is the ratio of the peaks of $N_{H_2}^{CO}$ and $N_{H_2}^{[C\,II]}$ over the shaded portions of the profiles. The uncertainties come from a Monte Carlo analysis over the range of temperature and densities considered.

X-ray-emitting plasma and the galaxy halo. The [O III]-emitting ionized gas, on the other hand, is more collimated (even narrower than the neutral material), has a lower outflow velocity (∼75 km s^{-1}), and is primarily photoionized by the starburst.

For the most part, the [C II] lines we measure have similar spectral shapes to the H I and/or CO (e.g., Figures 4 and 5), indicating that the [C II]-emitting gas is likely coupled to the neutral material and photoionized by the starburst. We do not see evidence for components of the [C II] line that do not correspond to either the H I or CO, except perhaps the most redshifted edge of the [C II] profile in pixel 1 (Figures 3, 4, and 5).

Another method to determine the fraction of [C II] associated with the ionized gas is to compare the [C II] intensity to that of the [N II] 205 μm line. The [N II] 205 μm line is only excited in the ionized ISM and it has a similar critical density to the [C II] 158 μm line. Using this method, Tarantino et al. (2021) found that the fraction of [C II] arising from the ionized medium is <12% in the disks of two normally star-forming galaxies. Unfortunately, there are no observations of the [N II] 205 μm line from either Herschel or SOFIA in M82. Contursi et al. (2013) used the [N II] 122 μm line to place limits on the fraction of [C II] arising from the ionized medium in the outflow at distances <1 kpc from the disk. Because the [C II] and [N II] 122 μm lines do not have similar critical densities,

these results are dependent on the electron density, which is largely unknown in the outflow of M82 (e.g., Shopbell & Bland-Hawthorn 1998; Yoshida et al. 2011). Nevertheless, Contursi et al. (2013) were able to constrain that ∼11%–40% of [C II] emission arises from the ionized gas in the southern outflow of M82 (at distances <1 kpc from the midplane). They note that these estimates will be even more uncertain when applied to regions with a complex mix of different ISM components, which is certainly the case in the outflow of M82. We can conclude, however, that the ionized gas is not the dominant contributor to the [C II] emission in the outflow of M82.

3.4. Synthesis

We summarize the contributions to the [C II] emission in the outflow of M82 from various ISM phases as follows. From our comparison of the H_2 column density measured from CO with that predicted from [C II], we find that ∼20% of the [C II] emission may arise from CO-emitting molecular gas (Figure 5). We attempt to quantify the contribution of CO-dark molecular gas, finding ∼4% of the total [C II] emission may arise from this phase. Therefore, ∼24% of the [C II] emission in the outflow of M82 may arise from the molecular ISM. For the contribution of ionized gas, we rely on measurements by Contursi et al. (2013) and estimate that ∼20% of the total [C II] emission may arise from the ionized ISM. Finally, we compare the H I column density measured from H I data with that predicted from [C II] and find that there is sufficient H I to fully explain the [C II] emission (Figure 4). Therefore, we can attribute the remaining ∼55% of the [C II] emission to the atomic ISM.

4. [C II] in the Disk of M82

As shown in Figures 1 and 2, we detect the [C II] line at high significance in the disk of M82. We calculate a total [C II] mass in the disk of $4 \times 10^6\ M_\odot$, calculated where S/N > 2 (Figure 2) following Equations (A5) and (A11).

In Figure 6, we compare representative [C II] and CO spectra in the disk of M82 at the center, at the peak of the [C II] emission, and on the redshifted and blueshifted sides of the galaxy. For this figure, we have spectrally smoothed the CO data to 10 km s^{-1} to match the [C II], convolved the [C II] data to the larger 22″ CO beam, and matched the pixel sizes. Both the CO and [C II] are reported in units of main-beam brightness temperature. We calculate the integrated intensity (moment 0) of the [C II] and CO on these matched data sets, as shown in Figure 6. Comparisons with the H I spectra are not possible because of deep absorption features in the H I over the region where the [C II] is detected in the disk (Section 2.2.2, Figure 1, and Martini et al. 2018). In general, we find that the CO and [C II] intensities and spectral shapes are quite similar, in agreement with previous work in this galaxy at lower resolution (e.g., Stacey et al. 1991).

In Figure 7, we make a position–velocity (PV) diagram of the matched-resolution CO and [C II] in the disk of M82. The velocities for both data sets are reported in the radio velocity convention and in the LSRK frame. We extract the [C II] and CO PV slices over the entire fully sampled region of the [C II] map, covering the central 3 kpc × 1 kpc of the galaxy along its major axis (Section 2.1.1). We collapse the PV slice along the minor axis by taking an average weighted by the intensity of each spaxel. Spaxels with intensities less than the rms noise of the cube (in areas away from emission) are removed.

As shown in Figure 7, the kinematics of the [C II] and CO generally agree in the inner regions of M82. In detail, however, there are some differences. The [C II] velocity appears to rise faster in the center than the CO. This disagreement is worse on the redshifted (i.e., eastern) side of the galaxy. The CO on this side of the galaxy appears more kinematically disturbed (e.g., Figure 2 of Leroy et al. 2015 and Figure 2 of Krieger et al. 2021). The H I, on the other hand, appears *less* kinematically disturbed on this side of the galaxy (e.g., Figure 1 of Martini et al. 2018). Therefore, if the [C II] in the disk primarily arises from the atomic gas (as it does in the outflow) then perhaps this could explain the kinematic differences we see in the PV diagrams, though this is somewhat speculative.

5. [C II] and CO throughout M82

5.1. [C II] and CO Luminosity Ratios

A somewhat different angle to assess the contribution of the molecular gas to the [C II] emission than presented in Section 3.2 is to compare the luminosity ratios of [C II] and CO. In principle, this ratio is sensitive to the FUV radiation field and the ability of CO to self-shield via dust from the FUV radiation (e.g., Accurso et al. 2017). To calculate the luminosities from the integrated intensities, we follow Equation (1) of Solomon et al. (1997):

$$L = 1.04 \times 10^{-3} \left[\frac{I_{\rm int}}{\rm Jy\ km\ s^{-1}}\right]\left[\frac{\nu(1+z)^{-1}}{\rm GHz}\right]\left[\frac{D_L}{\rm Mpc}\right]^2 L_\odot \quad (2)$$

where ν is the rest frequency of the line, z is the redshift, and D_L is the luminosity distance. Because M82 is very nearby, we take $D_L = 3.63$ Mpc and calculate $z = V_{\rm sys}/c$ with $V_{\rm sys} = 210$ km s^{-1} as the recessional velocity. We show these luminosities in Figure 8 for both the disk (blue–green filled contours) and outflow (teal circles; Table 2) of M82.

We compare the $L_{\rm [C\ II]}$ we infer from our measurements to those measured by Contursi et al. (2013). The region mapped by PACS extends farther into the outflow (∼1 kpc) than the upGREAT map (∼0.5 kpc), but not as far as the upGREAT outflow pointings. We match the PACS [C II] data to the IRAM 30 m CO data by first convolving the PACS cube to a 22″ Gaussian beam using the kernel provided by Aniano et al. (2011). We then match the pixel scales of the [C II] and CO cubes and re-derive the integrated intensities. We show the PACS [C II] and matched CO luminosities in Figure 8 as the grayscale contours. The PACS and upGREAT data agree well (as expected from the analysis in Section 2.1.1).

We compare the ratios we derive for M82 to a sample of 24 normally star-forming galaxies from the xCOLD GASS survey from Accurso et al. (2017) in Figure 8. In the disk of M82 we find somewhat lower $L_{\rm [C\ II]}/L_{\rm CO}$ ratios than for normally star-forming galaxies (the median for M82 is 0.4 dex lower). We note, however, that the measurements from Accurso et al. (2017) are galaxy-integrated, whereas the measurements from the disk of M82 are in ≈(125 pc)^2 regions (one pixel).

Another important caveat is that the galaxies studied by Accurso et al. (2017) tend to have metallicities less than solar, whereas M82 has solar (or slightly supersolar) metallicity (e.g., Lopez et al. 2020). Accurso et al. (2017) found the strongest

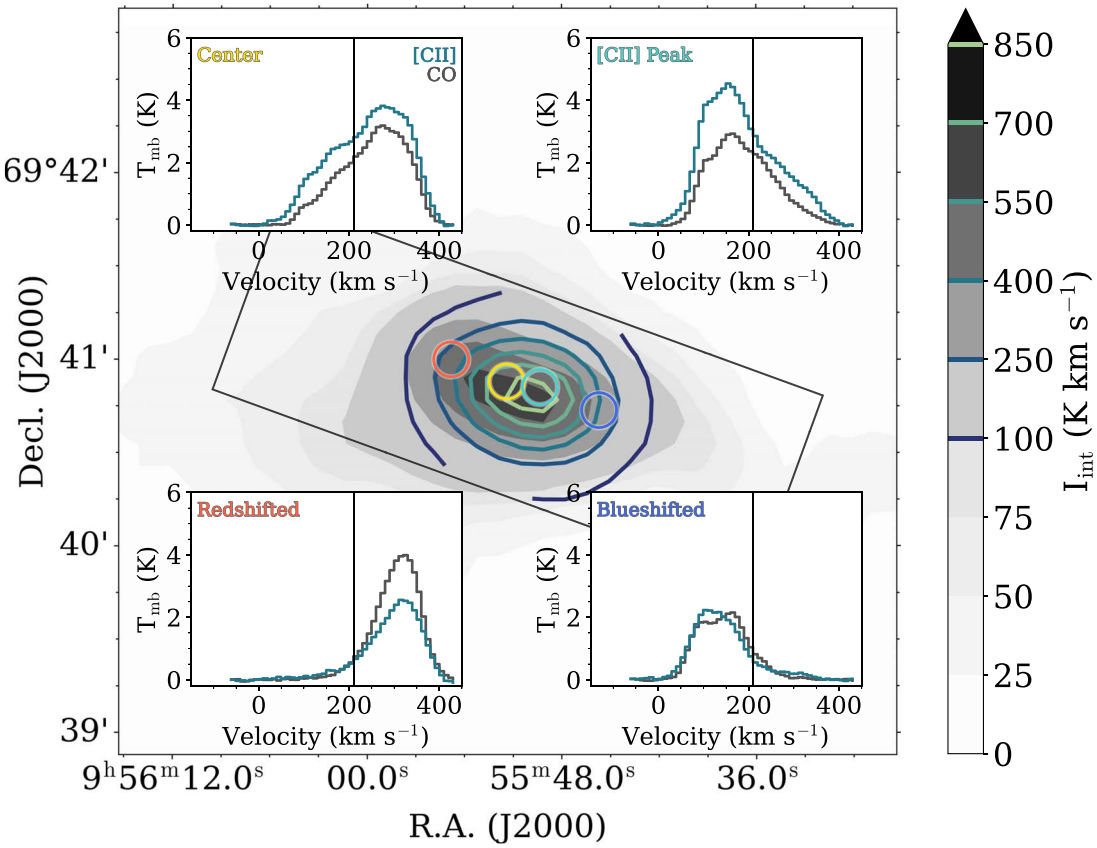

Figure 6. A comparison of the [C II] and CO spectra in the disk of M82. The grayscale filled contours show the CO integrated intensity. The blue–green open contours show the [C II] integrated intensities (see the lines in the color bar). The black rectangle marks the fully sampled region of the [C II] map. The subplots show the spectra of the CO (gray) and [C II] (teal) extracted at the galaxy center (yellow), at the peak of the [C II] emission (cyan), and on the redshifted and blueshifted sides of the galaxy (red, blue). Both the CO and [C II] intensities are reported as main-beam brightness temperatures, and the data sets have been matched to the same spatial and spectral gridding and convolved to the CO beam size (22″). The black vertical lines in the panels show V_{sys} = 210 km s^{-1}. Comparisons with H I are not possible to due strong absorption over this region (see Section 2.2.2).

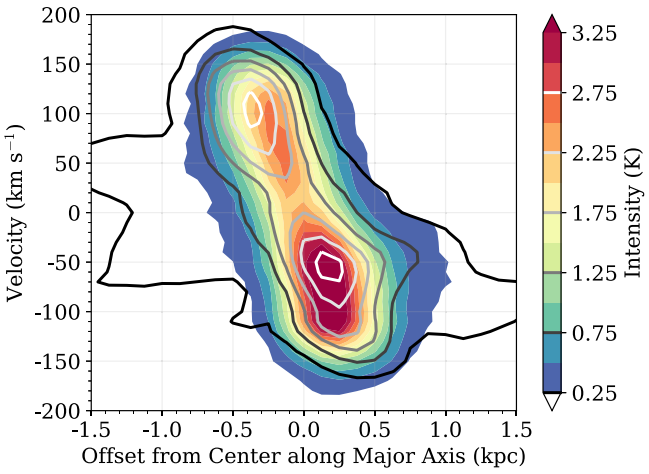

Figure 7. A PV diagram of the [C II] (filled colored contours) and CO (open grayscale contours) in the center of M82. This slice is extracted along the galaxy's major axis and covers the entire fully sampled region of the [C II] map (3 × 1 kpc). The CO and [C II] data have the same beam size, pixel scale, and velocity resolution. The *x*-axis shows the offset along the galaxy's major axis with respect to the center. The *y*-axis shows the velocity relative to V_{sys} = 210 km s^{-1} (Krieger et al. 2021). In general, the kinematics of the CO and [C II] agree, though the [C II] velocity rises faster than the CO in the center.

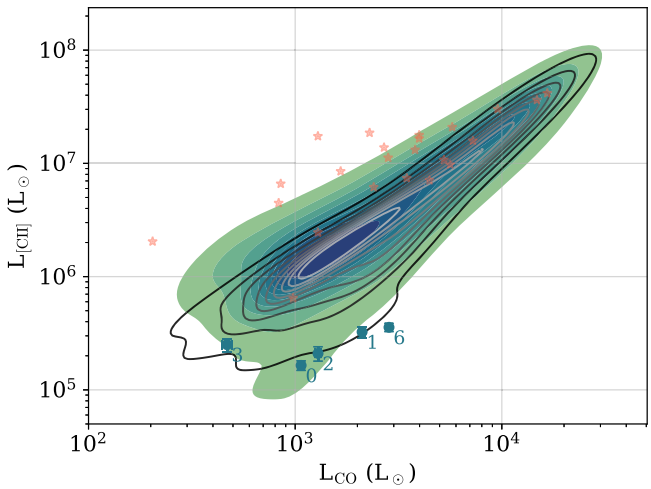

Figure 8. The CO and upGREAT [C II] luminosities in the disk (green–blue filled contours) and outflow (teal circles) of M82. The teal numbers indicate the pixel number of each outflow pointing. We compare our measurements to those from PACS (Contursi et al. 2013) in the grayscale contours. For all contours, the colors reflect the density of points. We also compare to integrated measurements from the xCOLD GASS survey of star-forming galaxies (red stars; Accurso et al. 2017).

trend in $L_{[C\,II]}/L_{CO}$ with metallicity (in 12 + log(O/H) units), where systems with higher metallicity have lower $L_{[C\,II]}/L_{CO}$. They also found a strong trend with the hardness of the radiation field (defined as the ratio of the FUV to near-UV flux), where harder radiation environments have lower $L_{[C\,II]}/L_{CO}$. Both of these trends may help explain why the

disk of M82 has lower $L_{[C\,II]}/L_{CO}$ than the star-forming galaxies analyzed by Accurso et al. (2017).

5.2. Fraction of [C II] in the Outflow of M82

At $z \sim 3$–7, recent observations with ALMA have revealed [C II] halos around some galaxies extending up to ∼10 kpc from the center and containing ∼50% of the [C II] emission (e.g., Fujimoto et al. 2019, 2020; Rybak et al. 2019; Ginolfi et al. 2020; Meyer et al. 2022, though see also Novak et al. 2020 for counter-examples). We note that these studies are a mix of detections from individual systems and stacks, as well as spatially unresolved and marginally resolved studies. Simulations have shown that these extended [C II] halos can be powered by supernova-driven cooling outflows (e.g., Pizzati et al. 2020).

As M82 is sometimes used as a local anchor for high-z star-forming galaxies, it is interesting to constrain the fraction of [C II] emission in the outflow compared to the disk. The CO in the outflow of M82 only extends for ∼2–3 kpc above and below the midplane (Walter et al. 2002; Salak et al. 2013; Leroy et al. 2015; Krieger et al. 2021). Martini et al. (2018) found that the H I is significantly more extended, reaching ∼5 kpc above the midplane and ∼10 kpc below (in the direction of M81, with which M82 is interacting; see also Yun et al. 1994). Based on lower-resolution CO data, Walter et al. (2002) measured $3.3 \times 10^8\ M_\odot$ of molecular gas in the halo and outflow of M82, $2.3 \times 10^8\ M_\odot$ in the disk, and $8.0 \times 10^8\ M_\odot$ in the tidal streamers, for a total molecular gas mass of $1.3 \times 10^9\ M_\odot$. We note that this total molecular gas mass agrees with other more recent measurements (Salak et al. 2013; Leroy et al. 2015; Krieger et al. 2021). Overall, Walter et al. (2002) found that while >70% of the molecular material resides outside the disk of M82, only ∼25% of the total molecular gas mass is swept up in the outflow/halo component with the rest being in the tidal streamers.

For the measurements of the [C II] halos at high z, outflow/halo and streamer components would be mixed together. However, as we know from M82, not all of this mass is outflowing, so attributing all of the extended [C II] emission to the outflow can significantly overestimate the [C II] mass outflow rates in these high-z systems. This rough comparison assumes that the [C II] and CO masses in each component track one another.

Because our upGREAT observations do not cover the full extent of the outflow of M82, we cannot directly measure the total [C II] extent, mass, or flux in the outflow relative to the disk. We will instead extrapolate our [C II] measurements to infer the total fraction of [C II] we might expect based on the CO. In the outflow, the average ratio of the peak brightness of the CO and the [C II] line (where [C II] is detected) is 2.0 ± 0.8, where the uncertainty is the standard deviation (see Figure 3). In the central disk, the peak brightness ratio is nearly the same, with an average and standard deviation of 2.1 ± 1.1 (see, e.g., Figure 6). We note that Walter et al. (2002) define the M82 disk as the inner 1 kpc, which is very similar to the region of the disk where we robustly detect [C II] emission (e.g., Figure 2). Therefore, since the ratio of the intensities in the central disk and outflow is roughly the same, we might expect the relative mass ratios to be the same as well. This means that we would expect to find ∼25% of the total [C II] in the outflow, ∼18% in the inner disk, with the remaining [C II] distributed in the streamers. Given that we measure a [C II] mass of $4 \times 10^6\ M_\odot$ in the disk (Section 4), we would predict $\sim 5.5 \times 10^6\ M_\odot$ of [C II] in the entire outflow of M82. This mass corresponds to a total integrated intensity of $\sim 3.5 \times 10^4$ K km s^{-1} (Equations (A11) and (A5)) and $L_{[C\,II]} \sim 1.7 \times 10^8\ L_\odot$ (Equation (2)).

Indeed, some observational studies of [C II] halos at high z do find evidence of an extended component but without a broad [C II] profile that would indicate an outflow (e.g., Novak et al. 2020; Spilker et al. 2020; Meyer et al. 2022). In particular, Spilker et al. (2020) studied molecular outflows in a sample of lensed dusty star-forming galaxies at $z > 4$. They found that >70% of the galaxies in their sample had clear evidence for a molecular outflow based on OH 119 μm absorption. However, none of these galaxies with confirmed molecular outflows had broad [C II] emission line wings. This suggests that, at least in this population of $z > 4$ highly star-forming galaxies, [C II] is not a robust tracer of outflowing molecular gas at high redshift.

In summary, in M82 we clearly detect [C II] in the starburst-driven outflow, though we expect that the outflowing [C II] accounts for only ∼25% of the total [C II] of the system. This is somewhat different than is observed for high-redshift [C II] outflows, where there is evidence for molecular outflows in broad emission lines but which lack robust [C II] (e.g., Novak et al. 2020; Spilker et al. 2020; Meyer et al. 2022).

6. FUV Radiation Field

Within PDRs, photoelectric heating of small dust grains efficiently heats the region and governs the chemistry, and this heating is primarily governed by the density (n) and the strength of the FUV radiation field (G/G_0;[21] e.g., Tielens & Hollenbach 1985; Wolfire et al. 1990). The intensities of lines emitted in a PDR are therefore sensitive to these properties as well, and line ratios of FIR fine structure lines and CO can be used to constrain n and G (e.g., Wolfire et al. 1990; Kaufman et al. 1999). In the center of M82, Kaufman et al. (1999) applied their PDR model to integrated measurements of FIR lines, finding $n \sim 10^4$ cm^{-3} and $G \sim 10^{3.5}\ G_0$. Contursi et al. (2013) also used the Kaufman et al. (1999) PDR model to measure the FUV radiation field in the central starburst and southern outflow of M82 (within 1 kpc of the midplane), finding $G = 10^{3.1-3.4}\ G_0$ in the starburst and $G \sim 10^{2.1}\ G_0$ in the outflow.

6.1. Radiation Field Constraints from CO and [C II]

From their PDR model, Kaufman et al. (1999) find that, while the ratio of the [C II] and CO integrated intensities (where both quantities are in units of erg s^{-1} cm^{-2} sr^{-1}) is mostly sensitive to the column density of C^+ and the temperature, this ratio does also depend on n and G (see their Figure 9). We therefore use the line ratios of [C II] and CO that we measure in the disk and outflow of M82 to place new constraints on the FUV radiation field in this region.

Figure 9 (left) shows the integrated intensity ratio of [C II] to CO. As has been found previously (e.g., Stacey et al. 1991; Kaufman et al. 1999), ratios range from $\sim 3 \times 10^3$ to 7×10^3 in the disk of M82. Ratios in the outflow are substantially lower, with pixels 0, 1, 2, and 6 (purple colors in Figure 9 left) having ratios of 300–400.

Using the PDR model developed by Kaufman et al. (1999), we place limits on the strength of the FUV radiation field

[21] G_0 is the Habing field for radiation with energies from 6 to 13.6 eV, equivalent to 1.6×10^{-3} erg s^{-1} cm^{-2}.

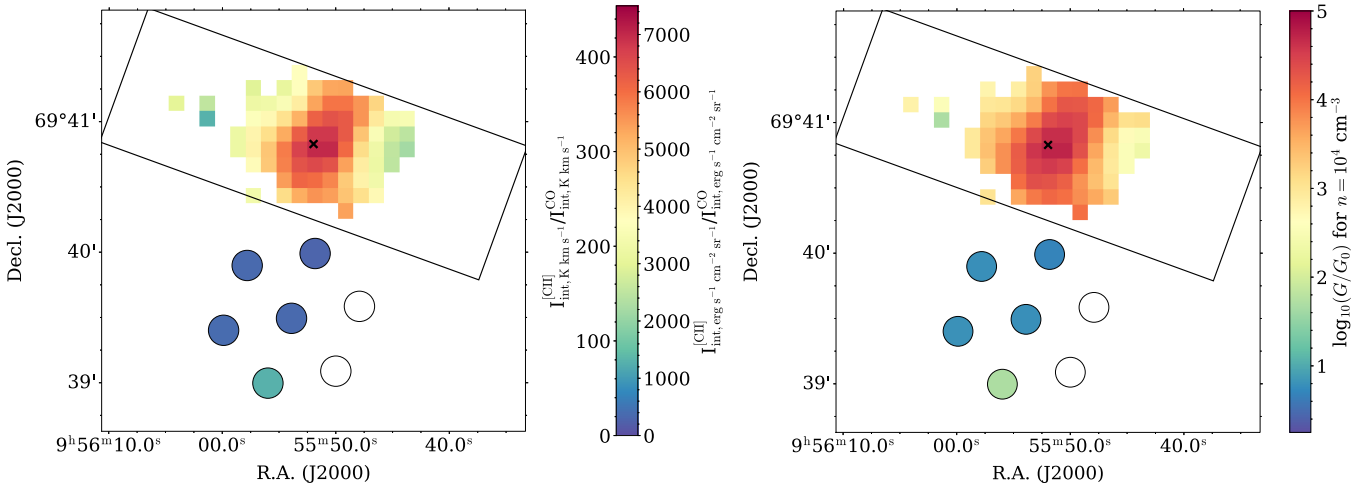

Figure 9. Left: the ratio of the [C II] to CO integrated intensities (in units of erg s^{-1} cm^{-2} sr^{-1} and K km s^{-1}), in the same style as Figure 2. In the disk, the [C II] and CO data cubes, from which the integrated intensities are calculated, have the same beam size, pixel scale, and velocity resolution (see Section 4). Right: the estimated strength of the FUV radiation field based on the PDR model by Kaufman et al. (1999) using the ratios from the left plot and assuming a density of 10^4 cm^{-3}.

assuming some density of the material. We interpolate the predictions of the Kaufman et al. (1999) PDR model (their Figure 9) to estimate G for a given [C II]-to-CO intensity ratio. This estimation of G is shown in Figure 9 (right). For a fiducial density of $n = 10^4$ cm^{-3} (following the results of Kaufman et al. 1999), the observed [C II]/CO ratios in the disk can be explained by $G \sim 10^{3-5}\,G_0$, in agreement (though somewhat circularly) with Kaufman et al. (1999) and Contursi et al. (2013).

In the outflow, we estimate a much lower FUV radiation field, with pixels 0, 1, 2, and 6 (blue colors in Figure 9 right) having $G \sim 6\,G_0$. Although the outflow is less dense than the disk (e.g., Yuan et al. 2023), the result of a much smaller FUV radiation field holds (see Section 6.2 for more discussion on the effect of uncertainties in the assumed density).

6.2. Uncertainties on G/G$_0$ due to the Assumed Density

A major source of uncertainty in these calculations is the assumed density (n). While we assume a fiducial $n = 10^4$ cm^{-3} motivated by the results of Kaufman et al. (1999) in the center of M82, it is unlikely that the outflow is this dense (as discussed in Section 3 and in Contursi et al. 2013).

In the disk, we allow the assumed density to vary by 0.5 dex (i.e., $n = 10^{3.5-4.5}$ cm^{-3}). Because the PDR models are not monotonic with density (see Figure 9 of Kaufman et al. 1999), we perform a grid search in steps of 0.1 dex in density and find the minimum and maximum values of G/G_0 at each disk pixel. For the disk, the uncertainty at each pixel is roughly the same ($\log_{10}(G/G_0)^{+0.5}_{-0.6}$).

In the outflow, the density is almost certainly much lower than 10^4 cm^{-3}. We employ the same grid search as described above over a range of $n = 10^{2-4}$ cm^{-3}. The lower limit encompasses the density limits determined by Contursi et al. (2013) and used in Section 3.1. We assume that our fiducial density is the maximum density in the outflow. The lower uncertainty on G/G_0 in the outflow comes from allowing the assumed density to be 2 dex lower than the fiducial assumption (i.e., $n = 10^{2-4}$ cm^{-3}).

Accounting for the density uncertainties, we find $G/G_0 \approx 10^{1.8-5.2}$ in the disk and $G/G_0 \approx 10^{0.1-1.0}$ in the outflow (excluding each green point in the disk and outflow). Therefore, even considering the uncertainties from the density assumptions, the radiation field in the outflow is substantially lower than that in the disk.

7. Summary

M82 is an archetypal example of a starburst-driven outflow and is an ideal laboratory in which to study the detailed physics of superwinds. Here, we present new velocity-resolved observations of the [C II] 158 μm emission line toward the center and southern outflow of M82, enabled by upGREAT on board SOFIA. With upGREAT, we mapped the central 3 kpc × 1 kpc of the disk of M82. In the southern outflow, we use one pointing of the seven-pixel upGREAT array to measure [C II] at distances of 1–2 kpc from the midplane (Figure 1). Below we summarize the main results of this analysis, indicating the relevant figures and/or tables.

1. We detect the [C II] line out to 2 kpc from the midplane along the southern outflow at 10 km s^{-1} velocity resolution (Figure 3). This is twice as far as previously probed by Herschel PACS (Contursi et al. 2013; Herrera-Camus et al. 2018).
2. We compare the column densities of the atomic medium measured from the H I data to the CNM column density measured from the [C II] spectra (Figure 4). Similarly, we compare the column densities of the molecular medium measured from the CO data to the H_2 column density measured from the [C II] spectra (Figure 5). From these comparisons, we find that the majority (>55%) of the [C II] arises from the atomic component. It is likely that the molecular gas (including an estimate of the CO-dark molecular gas) contributes ∼25% and that the ionized gas contributes ∼20% of the [C II] emission.
3. We are able to extend the results from Walter et al. (2002) from CO to estimate the total fraction of [C II] in the outflow of M82. While the bulk of the [C II]-emitting gas is likely outside the main disk, only a small fraction is actually outflowing (with the rest located in tidal streamers, for example). This may help inform observations of [C II] halos at higher redshifts, which sometimes lack outflow signatures.

4. We estimate the strength of the FUV radiation field in the disk and outflow of M82 using the PDR model developed by Kaufman et al. (1999). In the disk of M82, we find $G \sim 10^{3-5}\,G_0$, in agreement with previous measurements (Figure 9; Kaufman et al. 1999; Contursi et al. 2013). The FUV radiation field we measure ∼1.5 kpc away from the disk in the outflow, however, is 2–3 orders of magnitude lower than that in the disk.

Owing to the sensitivity and wavelength coverage of ALMA, the [C II] 158 μm emission line is routinely observed in galaxies at $z \gtrsim 2$. Because this line is bright, it is a more attractive tracer of molecular gas than CO in these systems. However, it is crucial to understand the contribution of the various ISM phases to the [C II] line in order to use this line as a tracer of molecular gas and star formation. The galaxy systems studied so far at $z \gtrsim 2$ tend to have high star formation rates, so understanding the behavior of the [C II] line in this starburst environment is critical to inform these high-z measurements. Unfortunately, with the end of the SOFIA mission, observations of [C II] and other FIR lines in the local Universe will be possible only with balloon missions for at least the next few decades. Future facilities in space are needed to more completely understand how the various ISM phases contribute to the [C II] 158 μm line as a function of spatial resolution, environment, and ISM conditions.

Acknowledgments

R.C.L. acknowledges support for this work provided by NASA through award number 08-0225 issued by the Universities Space Research Association, Inc. (USRA) and by a National Science Foundation (NSF) Astronomy and Astrophysics Postdoctoral Fellowship under award AST-2102625. A.D.B. acknowledges support from the NSF under award AST-2108140. R.H.-C. thanks the Max Planck Society for support under the Partner Group project "The Baryon Cycle in Galaxies" between the Max Planck for Extraterrestrial Physics and the Universidad de Concepción. R.H.-C. also gratefully acknowledges financial support from Millennium Nucleus NCN19058 (TITANs), and ANID BASAL projects ACE210002 and FB210003. This work is based on observations made with the NASA/DLR Stratospheric Observatory for Infrared Astronomy (SOFIA), project #08_0225. SOFIA is jointly operated by USRA, under NASA contract NNA17BF53C, and the Deutsches SOFIA Institut (DSI) under DLR contract 50 OK 2002 to the University of Stuttgart. This work is based on observations carried out under project No. 107-19 with IRAM 30 m telescope. IRAM is supported by INSU/CNRS (France), MPG (Germany), and IGN (Spain). The National Radio Astronomy Observatory is a facility of the National Science Foundation operated under cooperative agreement by Associated Universities, Inc. This research has made use of the NASA/IPAC Extragalactic Database (NED), which is funded by the National Aeronautics and Space Administration and operated by the California Institute of Technology. This research has made use of NASA's Astrophysics Data System Bibliographic Services.

Facilities: SOFIA (upGREAT), IRAM:30m, VLA, GBT.

Software: Astropy (Astropy Collaboration et al. 2018, 2022), *kalibrate* (Guan et al. 2012), MatPlotLib (Caswell et al. 2020), NumPy (Harris et al. 2020), pandas (Reback et al. 2020), photutils (Bradley et al. 2021), SciPy (Virtanen et al. 2020), seaborn (Waskom et al. 2014), spectral-cube (Ginsburg et al. 2019), WebPlotDigitizer (Rohatgi 2021).

Appendix
Calculating the C^+ Density and Mass in the Outflow

We calculate the [C II] density and mass in the outflow of M82 channel-by-channel for the velocity-resolved [C II] spectrum. We describe this calculation below and direct the reader to Goldsmith et al. (2012) and Tarantino et al. (2021, and references therein) for a much more complete discussion. We note that these calculations assume the [C II] is optically thin, which is well supported by the results of Contursi et al. (2013).

First, we can relate the column density of C^+ (N_{C^+}) to the [C II] intensity ($I_{[C\,II]}$) in each channel of the spectrum:

$$N_{C^+} = \frac{3.0 \times 10^{15}}{B}\left[\frac{I_{[C\,II]}}{\mathrm{K}}\right]\left[\frac{\Delta V}{\mathrm{km\ s^{-1}}}\right]\mathrm{cm^{-2}} \tag{A1}$$

where

$$B = \frac{2e^{-91.2/T}}{1 + 2e^{-91.2/T} + A_{ul}/(\Sigma R_{ul} n_i)} \tag{A2}$$

and where ΔV is the channel width in km s^{-1}, T is the kinetic temperature in K, A_{ul} is the Einstein A spontaneous decay rate (2.3×10^{-6} s^{-1} for the 158 μm transitions of [C II]), and $\Sigma R_{ul} n_i$ is the sum over all i collisional partners with collisional decay rates R_{ul} and volume densities n_i (Crawford et al. 1985; Goldsmith et al. 2012; Tarantino et al. 2021).

A.1. Collisions with Atomic Gas

First, we focus on collisions with the atomic gas only. In particular, the [C II] is excited primarily in the CNM (e.g., Pineda et al. 2013; Fahrion et al. 2017; Herrera-Camus et al. 2017; Tarantino et al. 2021). Therefore, the sum over the collisional partners in Equation (A2) can be simplified to include only neutral hydrogen and helium:

$$\begin{aligned}\Sigma R_{ul,i} n_i &= n_{CNM}[R_{ul}(H^0) + R_{ul}(He^0)]\ \mathrm{s^{-1}} \\ &= 1.038 R_{ul}(H^0) n_{CNM}\ \mathrm{s^{-1}}\end{aligned} \tag{A3}$$

where we have made the final simplification because the collisional rate for helium is 38% of that for hydrogen (Draine 2011). Goldsmith et al. (2012) calculated that

$$R_{ul}(H^0) = 4.0 \times 10^{-11}(16 + 0.35T^{0.5} + 48T^{-1})\ \mathrm{cm^3\ s^{-1}}. \tag{A4}$$

We assume $T = 250$ K and $n = 100$ cm^{-3} following the results of Contursi et al. (2013, the discussion in Section 3). Therefore, $R_{ul}(H^0) = 9.1 \times 10^{-10}$ cm^3 s^{-1}, $\Sigma R_{ul,i} n_i = 9.4 \times 10^{-8}$ s^{-1}, and $B = 5.7 \times 10^{-2}$. With these assumptions, Equation (A1) becomes

$$N_{C^+;H^0} = 5.2 \times 10^{16}\left[\frac{I_{[C\,II]}}{\mathrm{K}}\right]\left[\frac{\Delta V}{\mathrm{km\ s^{-1}}}\right]\mathrm{cm^{-2}} \tag{A5}$$

considering only collisions with the atomic gas.

From $N_{C^+;H^0}$, we can estimate the effective CNM column density ($N_{CNM}^{[C\,II]}$) based on the relative abundance of carbon to hydrogen ($C/H = 1.5 \times 10^{-4}$; Gerin et al. 2015) assuming all

of the carbon is singly ionized and all the hydrogen is atomic:

$$N_{\rm CNM}^{\rm [C\,II]} = \frac{N_{\rm C^+;H^0}}{\rm C/H}. \quad \text{(A6)}$$

The warm phase of the H I accounts for 30%–70% of the H I emission (Heiles & Troland 2003) but does not contribute to the [C II] emission (e.g., Pineda et al. 2013; Fahrion et al. 2017; Herrera-Camus et al. 2017). We show this effective CNM column density profile based on the [C II] in Figure 4 (teal).

A.2. Collisions with Molecular Gas

Next, we consider collisions with the molecular gas, H_2. In this case, the sum over the collisional partners in Equation (A2) can be simplified to include only molecular hydrogen:

$$\Sigma R_{{\rm ul},i} n_i = n_{\rm mol} R_{\rm ul}({\rm H_2})\ {\rm s^{-1}}. \quad \text{(A7)}$$

Goldsmith et al. (2012) calculated that

$$R_{\rm ul}({\rm H_2}) = 3.8 \times 10^{-10} \left(\frac{T}{100}\right)^{0.14} {\rm cm^3\ s^{-1}} \quad \text{(A8)}$$

where T is again the kinetic temperature in K. Using the same assumed temperature and density as above, $R_{\rm ul}({\rm H_2}) = 4.5 \times 10^{-10}\,{\rm cm^3\ s^{-1}}$, $\Sigma R_{{\rm ul},i} n_i = 4.5 \times 10^{-8}\ {\rm s^{-1}}$, and $B = 2.9 \times 10^{-2}$. With these assumptions, Equation (A1) becomes

$$N_{\rm C^+}^{\rm H_2} = 1.0 \times 10^{17} \left[\frac{I_{\rm [C\,II]}}{\rm K}\right] \left[\frac{\Delta V}{\rm km\ s^{-1}}\right] {\rm cm^{-2}} \quad \text{(A9)}$$

considering only collisions with the molecular gas.

From $N_{\rm C^+;H_2}$, we can estimate the effective H_2 column density ($N_{\rm H_2}^{\rm [C\,II]}$) based on the relative abundance of carbon to H_2 ($\rm C/H_2 = 7.5 \times 10^{-5}$; i.e., half the C/H ratio from Gerin et al. 2015) assuming all of the carbon is singly ionized and all the hydrogen is molecular:

$$N_{\rm H_2}^{\rm [C\,II]} = \frac{N_{\rm C^+}^{\rm H_2}}{\rm C/H_2}. \quad \text{(A10)}$$

We show this effective H_2 column density profile based on the [C II] in Figure 5 (teal).

A.3. C^+ Mass Estimate

From the C^+ column density calculated from Equation (A5) (since most of the [C II] is excited through collisions with atomic gas), we calculate the total C^+ mass ($M_{\rm C^+}$) in each upGREAT pointing in the outflow. In each LFA pixel,

$$M_{\rm C^+} = 2.2 \left[\frac{A_{\rm pix}}{\rm arcsec^2}\right] \left[\frac{d}{\rm Mpc}\right]^2 \left[\frac{\sum_v N_{\rm C^+}}{10^{18}\ {\rm cm^{-2}}}\right] M_\odot \quad \text{(A11)}$$

where $A_{\rm pix}$ is the area of each LFA pixel ($\approx 156''^2$), d is the distance to the galaxy in Mpc, and $\sum_v N_{\rm C^+}$ is the sum of the C^+ column density over all of the channels. We report $M_{\rm C^+}$ in each LFA pixel in the pointing along the outflow in Table 1. The total C^+ mass measured in these observations of the outflow is $4.2 \times 10^4\ M_\odot$ (excluding pixels 4 and 5, where the [C II] line is not detected). $M_{\rm C^+}$ changes by a factor of $\sim$2 for a factor of 2 change in either the assumed CNM temperature (T) or density ($n_{\rm CNM}$).

ORCID iDs

Rebecca C. Levy https://orcid.org/0000-0003-2508-2586
Alberto D. Bolatto https://orcid.org/0000-0002-5480-5686
Elizabeth Tarantino https://orcid.org/0000-0003-1356-1096
Adam K. Leroy https://orcid.org/0000-0002-2545-1700
Lee Armus https://orcid.org/0000-0003-3498-2973
Kimberly L. Emig https://orcid.org/0000-0001-6527-6954
Rodrigo Herrera-Camus https://orcid.org/0000-0002-2775-0595
Daniel P. Marrone https://orcid.org/0000-0002-2367-1080
Elisabeth Mills https://orcid.org/0000-0001-8782-1992
Oliver Ricken https://orcid.org/0000-0002-2155-3259
Juergen Stutzki https://orcid.org/0000-0001-7658-4397
Sylvain Veilleux https://orcid.org/0000-0002-3158-6820
Fabian Walter https://orcid.org/0000-0003-4793-7880

References

Accurso, G., Saintonge, A., Catinella, B., et al. 2017, MNRAS, 470, 4750
Aniano, G., Draine, B. T., Gordon, K. D., & Sandstrom, K. 2011, PASP, 123, 1218
Astropy Collaboration, Price-Whelan, A. M., Lim, P. L., et al. 2022, ApJ, 935, 167
Astropy Collaboration, Price-Whelan, A. M., Sipőcz, B. M., et al. 2018, AJ, 156, 123
Beirão, P., Armus, L., Lehnert, M. D., et al. 2015, MNRAS, 451, 2640
Bolatto, A. D., Wolfire, M., & Leroy, A. K. 2013, ARA&A, 51, 207
Bradley, L., Sipocz, B., Robitaille, T., et al. 2021, astropy/photutils: v1.0.2, Zenodo, doi:10.5281/zenodo.4453725
Caswell, T. A., Droettboom, M., Lee, A., et al. 2020, matplotlib/matplotlib: REL: v3.3.2, Zenodo, doi:10.5281/zenodo.4030140
Contursi, A., Poglitsch, A., Graciá Carpio, J., et al. 2013, A&A, 549, A118
Crawford, M. K., Genzel, R., Townes, C. H., & Watson, D. M. 1985, ApJ, 291, 755
Croxall, K. V., Smith, J. D., Pellegrini, E., et al. 2017, ApJ, 845, 96
de Blok, W. J. G., Walter, F., Ferguson, A. M. N., et al. 2018, ApJ, 865, 26
Dessauges-Zavadsky, M., Ginolfi, M., Pozzi, F., et al. 2020, A&A, 643, A5
Draine, B. T. 2011, Physics of the Interstellar and Intergalactic Medium (Princeton, NJ: Princeton Univ. Press)
Engelbracht, C. W., Kundurthy, P., Gordon, K. D., et al. 2006, ApJL, 642, L127
Fahrion, K., Cormier, D., Bigiel, F., et al. 2017, A&A, 599, A9
Förster Schreiber, N. M., Genzel, R., Lutz, D., Kunze, D., & Sternberg, A. 2001, ApJ, 552, 544
Förster Schreiber, N. M., Genzel, R., Lutz, D., & Sternberg, A. 2003, ApJ, 599, 193
Freedman, W. L., Hughes, S. M., Madore, B. F., et al. 1994, ApJ, 427, 628
Fujimoto, S., Ouchi, M., Ferrara, A., et al. 2019, ApJ, 887, 107
Fujimoto, S., Silverman, J. D., Bethermin, M., et al. 2020, ApJ, 900, 1
Gerin, M., Ruaud, M., Goicoechea, J. R., et al. 2015, A&A, 573, A30
Ginolfi, M., Jones, G. C., Béthermin, M., et al. 2020, A&A, 633, A90
Ginsburg, A., Koch, E., Robitaille, T., et al. 2019, radio-astro-tools/spectral-cube: Release v0.4.5, Zenodo, doi:10.5281/zenodo.591639
Goldsmith, P. F., Langer, W. D., Pineda, J. L., & Velusamy, T. 2012, ApJS, 203, 13
Grenier, I. A., Casandjian, J.-M., & Terrier, R. 2005, Sci, 307, 1292
Guan, X., Stutzki, J., Graf, U. U., et al. 2012, A&A, 542, L4
Harris, A. I., Güsten, R., Requena-Torres, M. A., et al. 2021, ApJ, 921, 33
Harris, C. R., Millman, K. J., van der Walt, S. J., et al. 2020, Natur, 585, 357
Heckman, T. M., Armus, L., & Miley, G. K. 1990, ApJS, 74, 833
Heiles, C., & Troland, T. H. 2003, ApJ, 586, 1067
Herrera-Camus, R., Bolatto, A., Wolfire, M., et al. 2017, ApJ, 835, 201
Herrera-Camus, R., Bolatto, A. D., Wolfire, M. G., et al. 2015, ApJ, 800, 1
Herrera-Camus, R., Sturm, E., Graciá-Carpio, J., et al. 2018, ApJ, 861, 94
Kaufman, M. J., Wolfire, M. G., Hollenbach, D. J., & Luhman, M. L. 1999, ApJ, 527, 795
Kennicutt, R. C. J., Armus, L., Bendo, G., et al. 2003, PASP, 115, 928
Krieger, N., Walter, F., Bolatto, A. D., et al. 2021, ApJL, 915, L3
Langer, W. D., Velusamy, T., Pineda, J. L., et al. 2010, A&A, 521, L17
Langer, W. D., Velusamy, T., Pineda, J. L., Willacy, K., & Goldsmith, P. F. 2014, A&A, 561, A122
Leroy, A. K., Walter, F., Martini, P., et al. 2015, ApJ, 814, 83

Levy, R. 2023, Supporting Code and Data for "[CII] Spectral Mapping of the Galactic Wind and Starbursting Disk of M82 with SOFIA" by Levy et al. 2023 v.1.0.0, Zenodo, doi:10.5281/zenodo.8400187
Loenen, A. F., van der Werf, P. P., Güsten, R., et al. 2010, A&A, 521, L2
Lopez, L. A., Mathur, S., Nguyen, D. D., Thompson, T. A., & Olivier, G. M. 2020, ApJ, 904, 152
Lynds, C. R., & Sandage, A. R. 1963, ApJ, 137, 1005
Madden, S. C., Geis, N., Genzel, R., et al. 1993, ApJ, 407, 579
Martini, P., Leroy, A. K., Mangum, J. G., et al. 2018, ApJ, 856, 61
McKeith, C. D., Castles, J., Greve, A., & Downes, D. 1993, A&A, 272, 98
Meyer, R. A., Walter, F., Cicone, C., et al. 2022, ApJ, 927, 152
Mookerjea, B., Israel, F., Kramer, C., et al. 2016, A&A, 586, A37
Nagao, T., Maiolino, R., Marconi, A., & Matsuhara, H. 2011, A&A, 526, A149
Novak, M., Venemans, B. P., Walter, F., et al. 2020, ApJ, 904, 131
Pineda, J. L., Langer, W. D., Velusamy, T., & Goldsmith, P. F. 2013, A&A, 554, A103
Pizzati, E., Ferrara, A., Pallottini, A., et al. 2020, MNRAS, 495, 160
Reback, J., McKinney, W., jbrockmendel, et al. 2020, pandas-dev/pandas: Pandas v1.1.3, Zenodo, doi:10.5281/zenodo.4067057
Risacher, C., Güsten, R., Stutzki, J., et al. 2018, JAI, 7, 1840014
Rohatgi, A., 2021 ankitrohatgi/WebPlotDigitizer: Version 4.1 of WebPlotDigitizer v4.1,, Zenodo, doi:10.5281/zenodo.592175
Röllig, M., Simon, R., Güsten, R., et al. 2016, A&A, 591, A33
Rybak, M., Calistro Rivera, G., Hodge, J. A., et al. 2019, ApJ, 876, 112
Salak, D., Nakai, N., Miyamoto, Y., Yamauchi, A., & Tsuru, T. G. 2013, PASJ, 65, 66
Shopbell, P. L., & Bland-Hawthorn, J. 1998, ApJ, 493, 129
SINGS Team 2020, Spitzer Infrared Nearby Galaxy Survey, IPAC, doi:10.26131/IRSA424
Solomon, P. M., Downes, D., Radford, S. J. E., & Barrett, J. W. 1997, ApJ, 478, 144
Spilker, J. S., Phadke, K. A., Aravena, M., et al. 2020, ApJ, 905, 85
Stacey, G. J., Geis, N., Genzel, R., et al. 1991, ApJ, 373, 423
Strickland, D. K., & Heckman, T. M. 2009, ApJ, 697, 2030
Strickland, D. K., Ponman, T. J., & Stevens, I. R. 1997, A&A, 320, 378
Tarantino, E., Bolatto, A. D., Herrera-Camus, R., et al. 2021, ApJ, 915, 92
Temi, P., Hoffman, D., Ennico, K., & Le, J. 2018, JAI, 7, 1840011
Tielens, A. G. G. M., & Hollenbach, D. 1985, ApJ, 291, 722
Veilleux, S., Cecil, G., & Bland-Hawthorn, J. 2005, ARA&A, 43, 769
Veilleux, S., Maiolino, R., Bolatto, A. D., & Aalto, S. 2020, A&ARv, 28, 2
Veilleux, S., Rupke, D. S. N., & Swaters, R. 2009, ApJL, 700, L149
Virtanen, P., Gommers, R., Oliphant, T. E., et al. 2020, NatMe, 17, 261
Walter, F., Weiss, A., & Scoville, N. 2002, ApJL, 580, L21
Waskom, M., Botvinnik, O., Hobson, P., et al. 2014, Seaborn: V0.5.0 (November 2014) v0.5.0, Zenodo, doi:10.5281/zenodo.12710
Wolfire, M. G., Hollenbach, D., & McKee, C. F. 2010, ApJ, 716, 1191
Wolfire, M. G., Tielens, A. G. G. M., & Hollenbach, D. 1990, ApJ, 358, 116
Yamagishi, M., Kaneda, H., Ishihara, D., et al. 2012, A&A, 541, A10
Yoshida, M., Kawabata, K. S., & Ohyama, Y. 2011, PASJ, 63, 493
Yoshida, M., Kawabata, K. S., Ohyama, Y., Itoh, R., & Hattori, T. 2019, PASJ, 71, 87
Yuan, Y., Krumholz, M. R., & Martin, C. L. 2023, MNRAS, 518, 4084
Yun, M. S., Ho, P. T. P., & Lo, K. Y. 1994, Natur, 372, 530
Zanella, A., Daddi, E., Magdis, G., et al. 2018, MNRAS, 481, 1976